PFG – Journal of Photogrammetry, Remote Sensing and Geoinformation Science (2025) 93:583–609
https://doi.org/10.1007/s41064-025-00358-7

ORIGINAL ARTICLE

# The Invisible Plant: Estimating Fractional Vegetation Cover of *Tillandsia landbeckii* in the Atacama Desert using Hyperspectral EnMAP and High-Resolution Validation Data

**Fabian Reddig**[1] · **Christoph Hütt**[1] · **Alexander Jenal**[1,2] · **Jan Wolf**[1] · **Georg Bareth**[1]

Received: 10 December 2024 / Accepted: 17 August 2025 / Published online: 15 September 2025
© The Author(s) 2025

## Abstract

Fractional vegetation cover (FVC) is a critical canopy structural variable essential for understanding vegetation dynamics. Estimating FVC in arid environments often remains difficult due to sparse vegetation, weak spectral signals, and high spectral confusion with the background. This study investigates the potential of spaceborne imaging spectroscopy to overcome these limitations by estimating the FVC of *Tillandsia landbeckii*, a fog-dependent bromeliad endemic to the Atacama Desert. Owing to its low reflectance and lack of chlorophyll absorption features, *Tillandsia* remains largely undetectable using conventional multispectral sensors. We used hyperspectral data from the EnMAP satellite and applied six semi-supervised sparse spectral unmixing algorithms at both local and regional scales. Unlike traditional supervised approaches, our method does not rely on labeled training data. Instead, it uses a limited set of field- and image-based endmember spectra to perform subpixel unmixing. Validation was conducted using a high-resolution reference dataset combining a UAV orthomosaic (1.7 cm) and Pléiades Neo imagery (30 cm). While the best local model reached a mean absolute error (MAE) of 3.1%, restricting the regional regression to confirmed *Tillandsia* pixels further reduced the MAE to 1.8%. This study presents the first operational demonstration of EnMAP for subpixel mapping of *Tillandsia landbeckii* cover, highlighting the value of semi-supervised unmixing techniques for vegetation analysis in hyper-arid environments with limited reference data and strong spectral background similarity. The approach establishes a transferable framework for estimating low-signal vegetation in hyper-arid regions, advancing the state of the art in fractional cover mapping.

**Keywords** Remote sensing · Spectral unmixing · Hyperspectral · *Tillandsia landbeckii* · EnMAP

## 1 Introduction

The Atacama Desert is regarded as one of the oldest and driest regions on Earth (Dunai et al. 2005). A unique ecosystem that has adapted to its hyper-arid conditions is the so-called fog oasis (span. *Oasis de Niebla*) (Moat et al. 2021), which forms distinct vegetational patches approximately between 900 and 1200 m above sea level in a coastal strip about 3–45 km from the shoreline (Pinto et al. 2006). Within the fog-dependent ecosystems, the Bromeliaceae *Tillandsia landbeckii* (hereinafter referred to as *Tillandsia*) has evolved to thrive despite its restriction to specialized fog-dependent microhabitats and limited fog moisture availability (Mikulane et al. 2022). This plant relies almost exclusively on marine advective fog transported by southwest winds from the Pacific Ocean (Koch et al. 2022). Interwoven hairy and waxy leaves (epidermal trichomes) allow the plant to save water by absorbing fog and protecting itself from excessive

✉ Fabian Reddig
fabian.reddig@uni-koeln.de

Christoph Hütt
christoph.huett@uni-koeln.de

Alexander Jenal
alexander.jenal@uni-koeln.de

Jan Wolf
jwolf32@uni-koeln.de

Georg Bareth
g.bareth@uni-koeln.de

[1] GIS and Remote Sensing Group, Institute of Geography, University of Cologne, Albertus-Magnus-Platz, 50923 Cologne, Germany

[2] Application Center for Machine Learning and Sensor Technology, University of Applied Science Koblenz, Joseph-Rovan-Allee 2, 53424 Remagen, Germany

transpiration and solar radiation (Latorre et al. 2011; Males and Griffiths 2017). *Tillandsia* fields (tillandsiales), cover up to 1900 km$^2$ along the Pacific coast and are recognized as valuable bio-indicators of paleo fog variability in the Atacama Desert (e.g., Del Río et al. 2021; Jaeschke et al. 2019; Latorre et al. 2011; Moat et al. 2021; Pinto et al. 2006; Rundel et al. 1997). Although seemingly simple in structure, communities dominated by a single *Tillandsia* species play a crucial ecological role, reflecting past, present, and future changes in fog patterns and climate dynamics (Latorre et al. 2011; Mikulane et al. 2022; Rundel et al. 1997).

However, detecting and mapping tillandsiales across the Atacama Desert remains a significant challenge. This limitation arises not only from the scarcity of comprehensive field studies but also from the unique spectral and spatial characteristics of *Tillandsia* (Hesse 2012; Moat et al. 2021; Wolf et al. 2016).

As a typical Crassulacean Acid Metabolism (CAM) plant, *Tillandsia* exhibits lower photosynthetic activity (Jaeschke et al. 2024), and its epidermal trichomes act as a spectral barrier, obscuring chlorophyll beneath. Consequently, the species lacks the characteristic spectral patterns of green vegetation in the visible and near-infrared (VIS/NIR) domain (400–900 nm), including the typical red-edge slope around 720 nm (Fig. 1). In addition, *Tillandsia*'s overall reflectance is low, resulting in a weak spectral signal that often blends with the background, particularly under multispectral observation conditions. Previous studies have shown that the limited spectral resolution of multispectral satellite data prevents effective pixel-based classification of *Tillandsia* using spectral information alone, as the spectral contrast with the surrounding substrate is too weak to allow reliable detection (Mikulane et al. 2022).

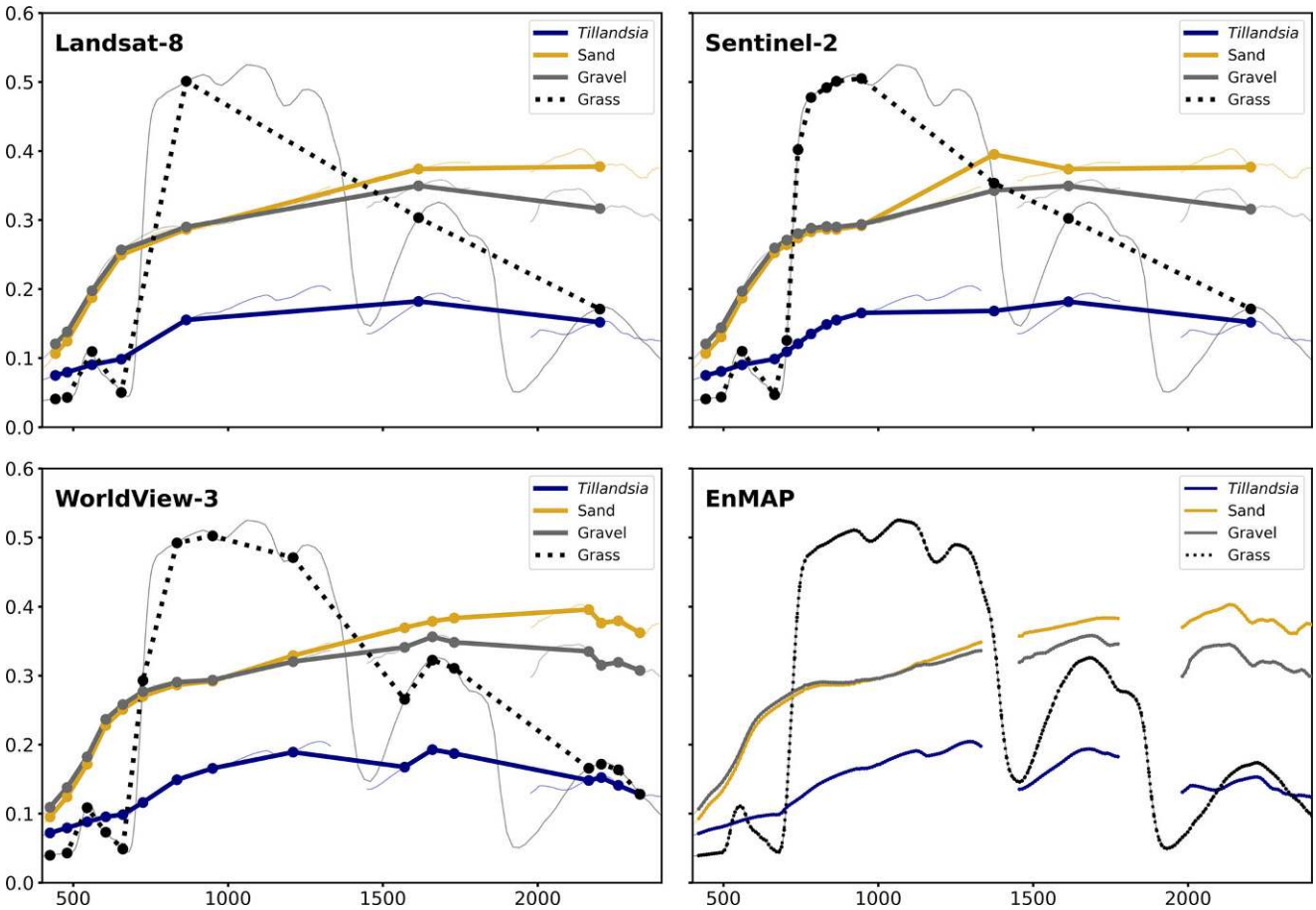


**Fig. 1** Spectral signatures of three surface types measured in the Atacama Desert (thin lines) resampled to the spectral resolution of various satellite sensors (thick lines). The spectra were obtained using a field-portable ASD FieldSpec 4 spectroradiometer. Colored dots overlaid on the spectra indicate the central wavelengths of each sensor band after spectral resampling. The comparison illustrates spectral gaps in multispectral sensors (Landsat-8, Sentinel-2, and WorldView-3), particularly in regions relevant for vegetation detection. Notably, the characteristic chlorophyll absorption features between 400–500 nm and the red absorption peak around 680 nm, typical of green vegetation, are largely absent or minimal in the *Tillandsia* spectrum. The grass spectrum, derived from the ASTER spectral library, is included as a reference for typical photosynthetically active vegetation and is not part of the study. The hyperspectral EnMAP sensor provides substantially higher spectral resolution and captures plant-characteristic absorption features more effectively than the multispectral systems

These spectral constraints are further compounded by the spatial limitations of many multispectral satellite sensors, which typically combine moderate spatial resolution with a limited number of broad spectral bands. Due to its sparse and linear growth patterns, *Tillandsia* often occupies only a fraction of a moderate resolution pixel, making reliable subpixel detection challenging. Although sensors such as WorldView-3, Landsat-8, and Sentinel-2 offer advantages in spatial or temporal resolution, their coarse spectral sampling and lack of distinctive spectral bands, particularly in the shortwave infrared (SWIR) domain, likely limit their ability to capture *Tillandsia*-characteristic spectral absorption features. Previous findings suggest that the combination of low vegetation cover and weak photosynthetic activity impedes reliable discrimination of *Tillandsia* using vegetation indices or multispectral feature-based classification approaches (Wolf et al. 2016). Although no specific studies have examined seasonal reflectance dynamics of *Tillandsia* to date, its perennial growth form and CAM physiology suggest limited seasonal variation in spectral properties, thereby reducing the potential benefit of frequent revisits. While multispectral sensors have enabled *Tillandsia* detection under certain conditions (see Sect. 2), their ability to reliably distinguish the species based solely on spectral reflectance, without spatial context or auxiliary classification steps, remains unsolved.

Thus, we consider *Tillandsia* to be effectively "invisible" to multispectral satellite sensors in the VIS/NIR domain due to its low fractional cover and the absence of strong chlorophyll absorption features. As suggested by Mikulane et al. (2022), hyperspectral data may overcome these limitations. This is supported by reflectance measurements collected using a field-portable spectroradiometer in March 2023. The spectra revealed distinct absorption features characteristic of *Tillandsia*, notably around 900 nm, 1200 nm, and 1450 nm, that clearly distinguish the plant from typical background substrates (Fig. 1). Many of these features lie in wavelength regions that are not covered, or only poorly represented, by standard multispectral sensors, particularly in the SWIR domain, and thus remained undetected in previous studies.

Building on these insights, this study pursues two interrelated objectives. First, we assess the potential of operational hyperspectral EnMAP data for estimating the fractional vegetation cover (FVC) of *Tillandsia landbeckii* in the Atacama Desert. As a key biophysical variable, FVC describes the proportion of ground covered by the aboveground vegetation and plays a central role in quantifying vegetation dynamics and ecosystem functioning (Liang and Wang 2020). Second, we explore how the composition of spectral libraries influences unmixing performance by comparing field-measured and image-derived endmembers within their respective modeling contexts.

To achieve these objectives, we employ a semi-supervised spectral unmixing approach that estimates subpixel vegetation fractions using a limited set of predefined endmembers. Unlike conventional machine learning methods that rely on extensive training data, this sparse unmixing framework yields data-efficient and transferable FVC estimates, particularly suited for remote ecosystems with spectrally weak and spatially fragmented vegetation. Critically, model validation is performed using a high-resolution, multi-source reference dataset that was created specifically for this purpose. It combines object-based classification from an ultra-high-resolution UAV orthomosaic (1.7 cm) and a pan-sharpened Pléiades Neo scene (30 cm), providing the spatial detail required to benchmark fractional cover estimates. To assess unmixing performance with respect to spectral library composition, we implement a dual-library design: in situ spectra are used for the local scale, while image-based endmembers are extracted directly from the EnMAP scene for the regional scale. This setup allows for an exploratory comparison of field-based and image-derived spectral libraries, highlighting their respective suitability and limitations under operational constraints.

By leveraging the full spectral capabilities of the EnMAP satellite, our approach addresses key limitations of previous multispectral systems. In doing so, this study develops a transferable and scalable framework for vegetation monitoring in dryland environments and demonstrates, for the first time, the operational feasibility of EnMAP for estimating subpixel *Tillandsia* cover.

## 2 Advancements in Remote Sensing of *Tillandsia landbeckii*

Initial remote sensing attempts to detect and estimate the distribution of *Tillandsia* ecosystems are mainly based on the visual interpretation of aerial photographs and extensive field surveys over several years. Pinto et al. (2006) developed a mapping approach based on digital cartography. They found that the distribution of tillandsiales is closely associated with the coastal topography and present fog corridors and significantly concentrates between 20°13′0″S and 20°48′0″S. Similarly, Hesse (2012) manually mapped *Tillandsia* using high-resolution Quickbird and GeoEye scenes. An algorithm-based classification was impossible due to the spectral similarity of *Tillandsia* to the surrounding bare ground and the complexity of their sparse vegetation patterns. With the increasing number of remote sensing satellites in orbit, replacing traditional, time-consuming, and labor-intensive methods with more efficient satellite-based approaches has become feasible. In an initial endeavor, Wolf et al. (2016) undertook the first effort to detect *Tillandsia* using high-resolution satellite scenes

**Table 1** Sensor characteristics and their role in the study workflow.

| Sensor | FieldSpec 4 | P4 RTK | Pléiades Neo (PNEO) | EnMAP |
|---|---|---|---|---|
| Number of bands | 2151 | 3 (RGB) | 7 | 246 |
| Spectral range | 350 to 2500 | RGB | 400 to 880 | 418 to 2445 |
| Bandwidth (nm) | 3 to 8 | – | 50 to 350 | 6 to 10 |
| Ground sampl. res. (m) | 0.28 | 0.017 | 0.3 (PAN)/1.2 (MS) | 30 |
| Date of acquisition | 04 March 2023 | 04 March 2023 | 04 March 2023 | 12 March 2024 |
| Usage | Reference | Reference | Reference | Prediction |

and high-resolution images from an unmanned aerial vehicle (UAV) at a local study site. They executed a two-step process involving supervised spatio-spectral classification and rule-based post-processing to identify tillandsiales from WorldView-3 satellite images. The sparse vegetation coverage and limited photosynthetic activity prevented the authors from successfully applying calculated spectral vegetation indices or complex models to the multispectral feature space to accurately distinguish *Tillandsia* from the surrounding bare ground. Instead, multi-scale segmentation and object-based feature extraction were used. Using 17 spatial and spectral features, the authors successfully detected and delineated the spatial patterns of tillandsiales. However, a limiting factor of the study was the relatively small size of the study area. To overcome this spatial limitation, Moat et al. (2021) aimed to map desert fog oasis ecosystems of Peru and Chile with images from the Moderate-resolution Imaging Spectroradiometer (MODIS) mission. However, despite the high spectral resolution, the low spatial resolution (250 m) and weak spectral signal necessitated manual mapping of *Tillandsia*. The signal they received from the Normalized Difference Vegetation Index (NDVI) was from herbaceous plants that responded to sporadic changes in moisture within the *Tillandsia* vegetation rather than from *Tillandsia* itself. However, based on identifying the characteristic longitudinal growth patterns in Google Earth and verifying them with georeferenced herbarium specimens, they successfully managed to map about 1900 km$^2$ of fog oasis. One step further, Mikulane et al. (2022) used WorldView-3 satellite images and a semi-automatic deep-learning approach to detect and classify tillandsiales. In general, their results are consistent with those of other authors, although the methodological approach, using multispectral data, also revealed significant limitations. In addition to the fact that shadows made classification more complex, especially at steep slopes, the authors also reported difficulties caused by the strong similarity of the *Tillandsia* spectrum to the surrounding inorganic substrate. The authors proposed utilizing hyperspectral images, which have more spectral bands, in higher spatial resolution as a potential data source to differentiate *Tillandsia* from other surfaces more effectively.

## 3 Material and Methods

To estimate the FVC of *Tillandsia landbeckii* in the Atacama Desert, we divided our analysis into two main parts: (i) generating the reference and validation data using classification results of the UAV-derived ultra-high-resolution orthomosaic and the multispectral pan-sharpened PNEO scene (Sect. 3.2), and (ii) applying linear spectral unmixing algorithms to the hyperspectral EnMAP scene based on two spectral libraries (Sect. 3.3) that account for spectral endmember variability. An overview of the data used in this study is provided in Table 1, and the overall workflow is illustrated in Fig. 2.

### 3.1 Study Area and Target Species

The coastal Atacama Desert extends west of the central Andes between 15°0′0″S and 25°0′0″S (Hampton 2001), crossing southern Peru and northern Chile (Fig. 3). With mean annual rainfall < 25 mm and partially even < 1 mm, it is often referred to as the driest non-polar desert on Earth (e.g., Bull et al. 2018; Eshel et al. 2021; Maßon et al. 2024). The extreme aridity results from the cold waters of the Humboldt Current, creating a thermal inversion that blocks coastal precipitation, intensified by the Andean rain shadow that restricts Amazonian moisture from reaching the Atacama Desert (Houston and Hartley 2003; Jimenez-Rodriguez et al. 2021).

The investigated tillandsiales are located at Cerro Oyarbide in the Tarapacá region of northern Chile, approximately 15 km from Iquique airport (20°29′51″S, 70°3′23″W) and around 20 km from the Pacific coast, at an elevation of approximately 1200–1260 m above sea level. The area is characterized by steep slopes and pronounced microtopography, which shape the distinct, linear vegetation bands of *Tillandsia*, oriented perpendicular to the incline (Koch et al. 2019). Vegetation cover is extremely sparse and composed almost exclusively of *Tillandsia landbeckii*. Field surveys and previous studies confirm the absence of other vascular plants within several kilometers of the site, with only isolated occurrences of lichens and xerothermic, drought-resistant mosses (Koch et al. 2019). The surrounding substrate consists mainly of bare mineral

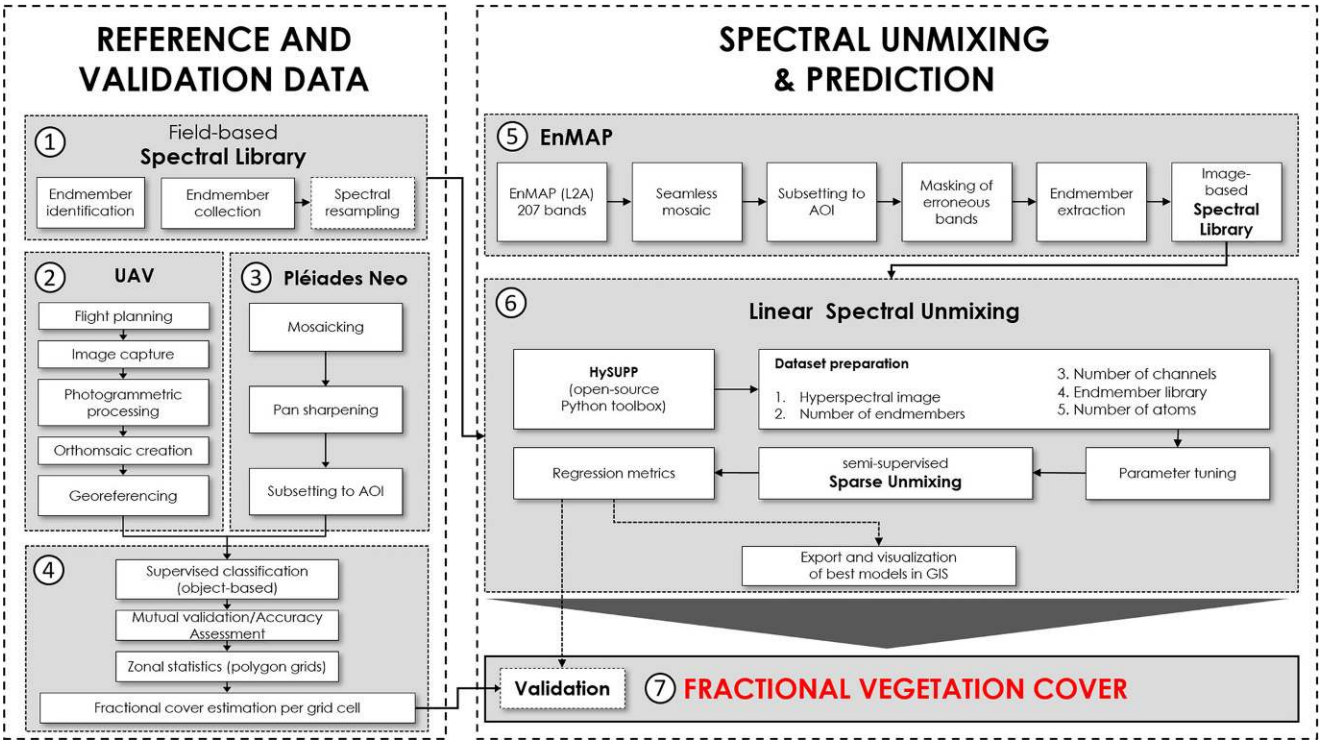


**Fig. 2** Workflow for FVC estimation of *Tillandsia* divided into seven steps: The process begins with step 1 and the collection of endmember spectra and the creation of a field-based spectral library. Steps 2 and 3 involve the processing and generation of our reference data. In step 4, the reference data is classified. Step 5 is dedicated to preparing the EnMAP image and the image-based spectral library. Step 6 involves executing six sparse spectral unmixing algorithms after parameter tuning. Finally, in step 7, the FVC of *Tillandsia* is validated against the reference data, and regression metrics are calculated

surfaces with no developed soil or organic layer. These open and homogeneous conditions, combined with the absence of competing plant species, make the site an ideal setting to isolate the spectral signal of *Tillandsia* and evaluate its spatial distribution.

The unique growth form of these vascular plants, along with roots that have no physiological function, allows them to stabilize in the bare sand (epiarenic growth), where they act as sand traps optimized for capturing fog moisture (Koch et al. 2022). They gather moisture and nutrients through specialized leaf hairs (trichomes), which give them a greyish appearance by refracting and absorbing light and blocking obscuring chlorophyll beneath. Another physiological adaptation for efficient water uptake is its use of an obligate CAM photosynthetic pathway, which enables nocturnal stomatal opening to fix carbon into malic acid when humidity is higher, minimizing water loss and optimizing water use efficiency (Haslam et al. 2003).

Our analysis targeted areas defined by the reference data, focusing on a local core area ($\sim 0.13$ km$^2$) where the ultra-high-resolution UAV orthomosaic was acquired for detailed insights, and on a regional core area ($\sim 110$ km$^2$) encompassing the extent of the high-resolution PNEO satellite scene for broader assessments (Fig. 3). This approach ensured a reliable evaluation of our unmixing methods at both local and regional scales. The field campaign was carried out in March 2023, during the austral autumn, under consistently clear-sky conditions, ensuring optimal atmospheric clarity for imaging spectroscopy observations.

## 3.2 Data Collection, Reference Generation, and EnMAP Preparation

### 3.2.1 Field Spectroradiometer Measurements

Spectral data were measured using the pistol grip of a field-portable FieldSpec-4 (model Hi-Res) spectroradiometer (Analytical Spectral Devices Inc., Boulder, Colorado, USA) positioned at nadir. The device, operating across a spectral range of 350 to 2500 nm, provided a field of view of 0.28 m at a height of 0.8 m during measurement. Following the manufacturer's recommendations, the spectroradiometer settings were optimized to match ambient solar illumination conditions, and the device was recalibrated every 10 to 15 min using a white reference panel. To reduce potential noise in the recorded spectra, spectrum averaging was set to 3.

In total, spectral data were collected at 210 points: 120 for *Tillandsia* and 30 each for sand, gravel, and roots. At each point, 10 measurements were averaged, resulting in

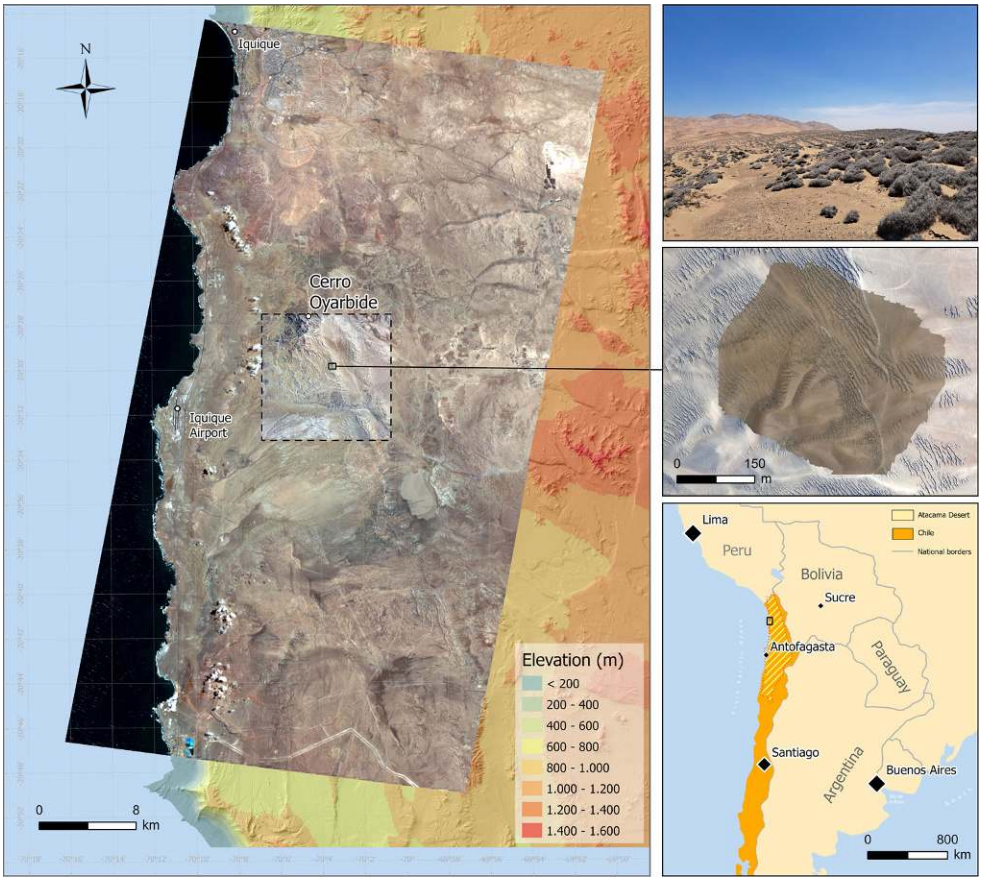


**Fig. 3** Left: EnMAP data product with dashed rectangle indicating the extent of the Pléiades NEO (PNEO) image and the regional investigation area used for estimating the FVC of *Tillandsia landbeckii*. The base layer shows a TanDEM-X digital elevation model at 12.5 m resolution. Middle right: Ultra-high-resolution orthomosaic acquired with a DJI Phantom 4 RTK. Top right: Photograph of *Tillandsia landbeckii* in its typical growth form and grey-silvery appearance at the Oyarbide study site. Bottom right: Overview map showing the location of the study area in the northern Atacama Desert, Chile

1200 spectra for *Tillandsia* and 300 spectra each for sand, gravel, and roots. Due to the high interspersion of *Tillandsia* roots with the substrate, the root spectra were excluded from the field-based spectral library, as it likely did not represent a pure spectrum, an essential requirement for library-based unmixing. Spectral data points were selected randomly without a predetermined sampling schema. For additional details on processing steps, refer to Sect. 3.3.2.

### 3.2.2 Creating an Ultra-High Resolution Orthomosaic

We used a DJI Phantom 4 RTK (P4 RTK) (DJI, Shenzhen, China) for the UAV-based image acquisition. The P4 RTK has a 1″ CMOS sensor capturing RGB images with 20 megapixels (Bareth and Hütt 2023). The flight was planned with an 80% side and 75% forward overlap covering 0.13 km$^2$ and executed on 04 March 2023. The mission was conducted 50 m above ground with a speed of 5 m/s. However, due to the varying terrain, the actual flight altitude fluctuated as the "Terrain Follow" mode was not activated. Our positioning accuracy was verified by surveying 13 Ground Control Points using a Topcon DGPS system with real-time kinematic (RTK) and Global Navigation Satellite Systems correction data. In total, 338 images were taken in nadir view. Data processing was done in Agisoft Metashape Professional version 2.1 (Agisoft LLC, St. Petersburg, Russia), resulting in a Digital Orthophoto (DOP) with a pixel spacing of 1.74 cm.

### 3.2.3 Generating a Pan-Sharpened Pléiades Neo Scene

Pléiades Neo (PNEO) is a high-resolution satellite constellation with a daily revisit time operated by Airbus Defence and Space. A cloud-free multispectral PNEO scene was acquired on 04 March 2023 (12 h 08 min 44 s PM CLST). The product packages include five multispectral bands with 1.2 m spatial and 12-bit radiometric resolution: deep blue (400–450 nm), blue (450–520 nm), green (530–590 nm), red (620–690 nm), red edge (700–750 nm), and near-infrared (770–880 nm). The panchromatic spectral band (450–800 nm) has a spatial resolution of 0.3 m. The scene was delivered as the highest processing level available for this dataset (ORTHO), orthorectified, geometrically projected to WGS84/UTM 19S, and radiometrically corrected to top-of-atmosphere reflectance. To enhance classification, we conducted a pan-sharpening resulting in a multispectral image with 0.3 m spatial resolution (Fig. 4).

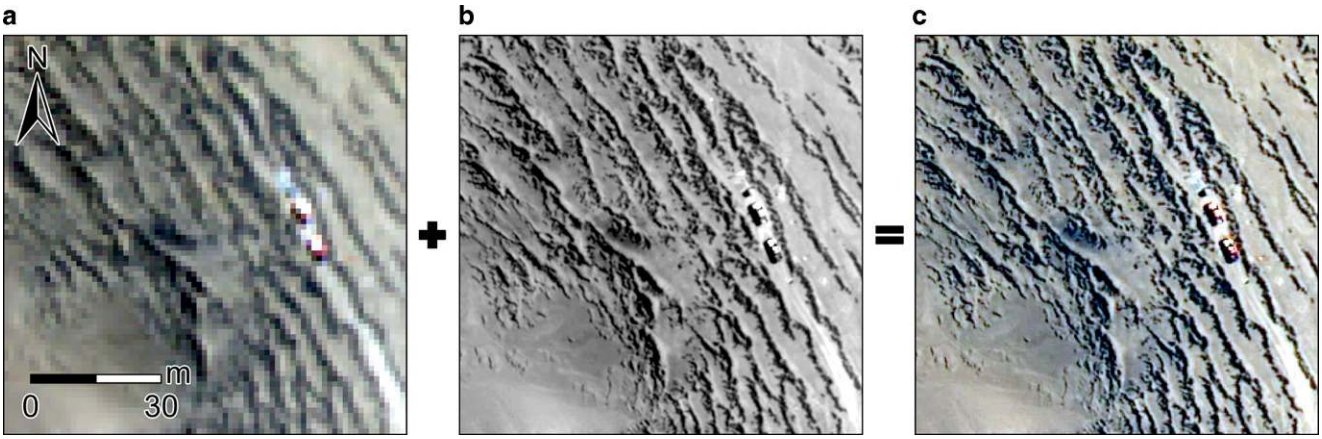


**Fig. 4** Manual pan-sharpening process. **a** RGB image with 1.2 m spatial resolution, **b** Panchromatic image with 0.3 m spatial resolution, **c** Pan-sharpened RGB image with 0.3 m spatial resolution

#### 3.2.4 Hyperspectral EnMAP Data

The Environmental Mapping and Analysis Program (EnMAP), a German hyperspectral satellite mission led by the German Aerospace Center (DLR), was launched in April 2022. EnMAP operates in a sun-synchronous orbit with a descending node equatorial crossing time of approximately 11:00 AM local solar time, ensuring consistent illumination conditions for acquisitions. Equipped with a pushbroom system, EnMAP provides spectral sampling at 6.5 nm in the VIS/NIR (420–1000 nm) and 10 nm in the SWIR (900–2450 nm). The satellite offers a ground sampling distance of 30 m. To match the atmospheric conditions observed in our field campaign in March 2023, we initially acquired an analysis-ready EnMAP image (L2A) on 16 March 2023. However, due to defects in this scene, we had to acquire two replacement scenes on 12 March 2024 (12:36:33 PM CLST). The images are geometrically projected using the WGS84/UTM 19S coordinate system and include radiometric and atmospheric correction (Chabrillat et al. 2022).

#### 3.2.5 Co-Registration and Classification

To ensure spatial alignment between all high-resolution reference datasets and the EnMAP scene, we used the pan-sharpened PNEO image as the geometric reference to align the UAV-based orthomosaic. A true rubber sheeting method ('spline transformation') was applied using 87 control points, primarily located on small *Tillandsia* shrubs due to the absence of other clearly distinguishable features. Although the EnMAP scene was not explicitly co-registered, its initial alignment was deemed satisfactory. No visible spatial shifts or misalignments were observed relative to the PNEO image, so additional adjustment was considered unnecessary.

In both the UAV orthomosaic and PNEO scenes, *Tillandsia* was classified using an object-based approach. The process involved segmenting pixels into homogeneous groups to incorporate spectral and spatial information. Higher-than-default values for spectral and spatial detail (both set to 18) were applied to enhance segmentation accuracy. A support vector machine (SVM) classifier was then trained for binary classification (*Tillandsia* vs. No *Tillandsia*) for each dataset.

Due to the nonparametric nature of the SVM classifier, a class balance was less critical compared to a statistical classifier (ESRI 2024). An independent validation was performed using 500 randomly generated points for the orthomosaic and 200 for the PNEO scene, selected with an equalized stratified random approach and manually verified for accuracy. While the UAV orthomosaic required no further re-classification step, the PNEO scene underwent a manual review, and misclassified areas, especially in shady, steep, and rugged slopes, were manually reclassified where needed.

To compare the classification results with those from the unmixing approach, a polygon grid with a 30 m cell size spatially congruent to the EnMAP scene was created (Bareth et al. 2016). Based on the grid, zonal statistics were derived by averaging the *Tillandsia* coverage of pixels from the orthomosaic and PNEO datasets within each grid cell. These statistics facilitate the calculation of descriptive metrics and histograms across specified zones (grid cells or pixels), enabling detailed spatial analysis. The reference *Tillandsia* cover fraction for each grid cell was determined by calculating the total area of *Tillandsia* polygons intersecting each cell, summing these intersection areas, and dividing by the total cell area. In addition, we used another grid with 60 m grid cell resolution and applied the same methodology. This aggregation was performed to smooth out fine-scale variability in the data and reduce the im-

pact of spatial misalignments between datasets, such as the reported EnMAP co-registration accuracy of 0.2 pixels (approximately 6 m), thereby enhancing the robustness of the derived zonal statistics (German Aerospace Center DLR). A similar 60 m aggregation approach was recently applied by Juola et al. (2024) to harmonize EnMAP and Sentinel-2 data for sensor intercomparison, minimizing spatial offsets and ensuring consistent reflectance statistics across resolutions. All EnMAP pixels (30 or 60 m) that lay fully within the bounds of the UAV orthomosaic (local) or pan-sharpened PNEO coverage (regional) were included in the validation. Pixel cells only partially overlapped by the high-resolution datasets were excluded to avoid incomplete reference data. Consequently, the validation dataset encompasses every pixel for which we could derive accurate fractional cover from the reference classification.

## 3.3 Linear Spectral Unmixing

### 3.3.1 Semi-Supervised Sparse Spectral Unmixing for FVC Estimation

The spectral response captured by imaging instruments typically represents a mixture of reflectance signals from different materials within the instantaneous field of view. Even high-resolution sensors may record such mixed signals when subpixel heterogeneity is present (Keshava and Mustard 2002). These so-called *mixed pixels* combine spectral information from multiple sources, making it challenging to directly identify individual materials (Adams et al. 1986). Spectral Unmixing (SU) addresses this challenge by decomposing each measured spectrum into a set of constituent spectra, referred to as *endmembers* (EM), and their corresponding fractional abundances, which indicate the proportion of each EM within the pixel (Keshava and Mustard 2002; Verrelst et al. 2023; Zare and Ho 2014). These EMs can be derived from field or laboratory measurements, pure pixels, or spectral libraries, and represent idealized signatures of distinct surface materials (Schowengerdt 2007). SU has been widely used since the early 1980s (Cavalli 2023) to identify and quantify subpixel components in mixed imagery. In this study, we employed *Linear Mixing Models*, which assume that the observed pixel spectrum is a linear combination of spatially distinct EMs, each contributing proportionally to its fractional area (Keshava and Mustard 2002).

Spectral variability, a significant challenge in SU, refers to the differences in spectral signatures of the same material, which can arise due to various intrinsic and extrinsic factors. Intrinsic factors include material composition, morphology, and physico-chemical variations, while extrinsic factors relate to object size, concentration, and environmental influences such as illumination or atmospheric distortion (Theiler et al. 2019). These variabilities can lead to inaccurate abundance fraction estimates and necessitate many EMs to represent mixed pixels (Borsoi et al. 2021; Theiler et al. 2019; Zare and Ho 2014; Zhou et al. 2020). As shown in Fig. 5, spectral differences can be substantial, driven by topographic effects and the precise subpixel composition of EMs. While averaging EM variations to create a single mean spectrum is one approach, it risks losing critical information and underrepresenting natural variability. To address these challenges, Sparse Spectral Unmixing (SSU) offers a robust alternative solution. SSU manages spectral variability by selecting a minimal set of spectral signatures from extensive libraries, framing the unmixing problem as a sparse regression. By accommodating multiple instances of the same material, SSU reduces the effects of variability while ensuring computational efficiency. Its sparsity constraints yield interpretable results, enhancing material identification in complex scenes (Borsoi et al. 2021; Iordache et al. 2014; Rasti and Koirala 2022).

### 3.3.2 Endmember Selection and Spectral Library Construction

To enable FVC estimation at both local and regional scales, we applied a dual-library approach. This strategy involved using two separate spectral libraries tailored to the spatial scale and data availability: a field-based library and an image-based library. The field-based spectral library, derived from in situ spectroradiometer measurements, was initially assumed to represent the most accurate and physically pure endmember signatures of *Tillandsia* and other surface types. These spectra, measured under controlled conditions and free from sensor-induced effects (Sect. 3.2.1), were expected to enable high-precision unmixing in the UAV-validated local area. For the regional scale, where pure *Tillandsia* pixels are absent and spectral variability is higher, we constructed an image-based spectral library from visually homogeneous areas in the EnMAP scene. To support endmember identification, we used high-resolution PNEO imagery as visual guidance, a common technique in spectral unmixing when higher-resolution data are available (Adams and Gillespie 2006).

The implementation of this approach involved two distinct spectral libraries. In the context of sparse spectral unmixing (SSU), such libraries are commonly referred to as bundles. These bundles include multiple spectral variants of the same material, allowing the unmixing algorithm to identify the best-matching signatures for each pixel (Borsoi et al. 2021). For clarity, we continue to use the term spectral library throughout this manuscript.

The first, referred to as the field-based spectral library for local-level unmixing, was created from in situ spectra measured during our field campaign (Sect. 3.2.1).

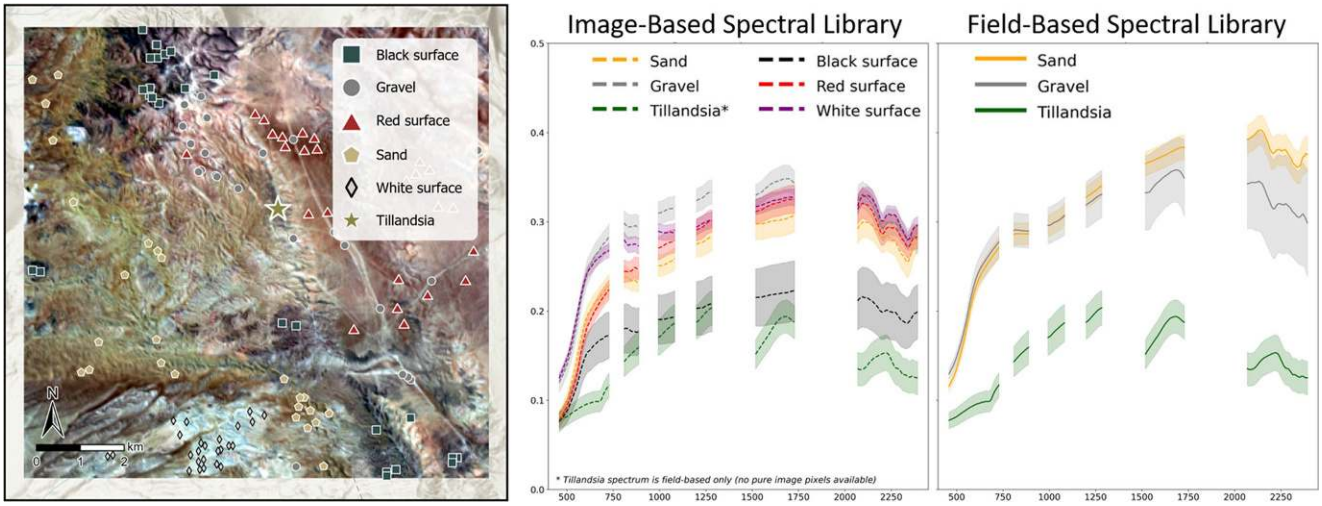


**Fig. 5** Locations of endmembers extracted from the EnMAP scene (left) for the image-based spectral library, based on visually homogeneous areas identified in the PNEO image. The center panel shows the image-based spectral library used for regional-scale unmixing, where *Tillandsia* spectra stem from in situ measurements (green star) and were resampled to match the spectral resolution of EnMAP. The right panel displays the field-based spectral library derived from in situ ASD measurements

The initial processing step involved adjusting the spectral resolution to align with that of EnMAP. Afterward, we removed bands affected by strong atmospheric water absorption (1294–1472 nm and 1810–1940 nm), excluded erroneous bands (424–454 nm, 734–801 nm, 895–982 nm, 1139–1187 nm, and 2400–2445 nm), and removed bands missing in the EnMAP image (1780–1967 nm). A Savitzky-Golay filter was then applied for smoothing and noise reduction using a 7-band window and a second-degree polynomial. The resulting library consisted of 147 remaining bands.

The second library, the image-based spectral library used for regional-level unmixing, was constructed by manually extracting five representative EMs from the EnMAP image. Given EnMAP's moderate spatial resolution, truly pure pixels are unlikely to exist. However, to approximate this condition, we used the high-resolution PNEO imagery to identify spatially homogeneous areas corresponding to the dominant surface types. These visually consistent patches were then matched to the corresponding EnMAP pixels, which we assumed to be spectrally dominated by a single material. For each surface type, 25 EnMAP spectra were collected to capture spectral variability (Fig. 5). Due to the narrow and fragmented growth pattern of *Tillandsia*, no EnMAP pixel was found to be dominated solely by the plant. Consequently, the *Tillandsia* EM from the field-based library, resampled to EnMAP spectral resolution, was incorporated into the image-based library. All preprocessing steps followed the same procedure as for the field-based library.

#### 3.3.3 Parameter Tuning and Implementation

Our unmixing workflow was performed using Python (v3.10.0) and a newly developed, open-source package called *HySUPP* ('HyperSpectral Unmixing Python Package') by Rasti et al. (2024). The package offers various unmixing methods with options for fine-tuning model parameters. We applied all six sparse representation-based algorithms provided by the package to estimate the FVC of *Tillandsia*. Parameter tuning was conducted via dedicated *.yaml* configuration files to optimize the performance of each model. We iterated through multiple parameter combinations in a loop, evaluating model outputs based on a combination of visual agreement with the reference data and quantitative accuracy metrics, including the coefficient of determination ($R^2$), mean absolute error (MAE), and root mean square error (RMSE). Details of the selected parameters and settings are provided in Table 2. The two best-performing models for the local and regional scales were selected based on overall accuracy, as detailed in the following Sect. 3.4.

### 3.4 Accuracy Assessment

For the machine-learning classification, we used a confusion matrix to derive standard accuracy metrics, including overall accuracy, user's accuracy, producer's accuracy, and the F1-score (Congalton and Green 2019). These metrics were computed separately for both classes (*Tillandsia* and non-*Tillandsia*) and for each data source, allowing for class-specific and source-specific assessment of classification performance.

**Table 2** List of unmixing algorithms from the HySUPP package, used for FVC estimations (based on and adapted from Rasti et al. (2024)). Columns three and four indicate the "best" parameters determined for our unmixing approaches at local and regional scales based on iterative testing and prior research.

| Acronym | *Algorithm | *Parameter (local) | *Parameter (regional) | Authors |
|---|---|---|---|---|
| SUnSAL | Sparse Spectral Unmixing by Variable Splitting and Augmented Lagrangian | AL_iters: 1000<br>lambd: $10^{-2}$<br>positivity: true<br>tol: $10^{-5}$ | AL_iters: 1000<br>lambd: $10^{-3}$<br>positivity: true<br>tol: $10^{-3}$ | Bioucas-Dias and Figueiredo (2010) |
| CLSUnSAL | Collaborative Sparse Unmixing by Variable Splitting and Augmented Lagrangian | AL_iters: 1000<br>lambd: $10^{-3}$<br>mu: 0.1<br>tol: $10^{-4}$ | AL_iters: 1000<br>lambd: $10^{-3}$<br>mu: 0.1<br>tol: $10^{-4}$ | Iordache et al. (2014) |
| $S^2$WSU | Spectral–Spatial Weighted Sparse Regression for Hyperspectral Image Unmixing | Lambd: $10^{-4}$ | Lambd: $10^{-5}$ | Zhang et al. (2018) |
| MUA SLIC | Fast Multiscale Spatial Regularization for Sparse Hyperspectral Unmixing | Beta: 2<br>lambda1: $10^{-5}$<br>lambda2: $10^{-5}$<br>slic_reg: $10^{-2}$<br>slic_size: 5 | Beta: $7 \cdot 10^{-3}$<br>lambda1: $10^{-1}$<br>lambda2: $10^{-3}$<br>slic_reg: $5 \cdot 10^{-3}$<br>slic_size: 3 | Borsoi et al. (2019) |
| SUnCNN | Sparse Unmixing Using Unsupervised Convolutional Neural Network | Exp_weight: 0.99<br>lr: $10^{-3}$<br>niters: 1000<br>noisy_input: false | Exp_weight: 0.99<br>lr: $10^{-3}$<br>niters: 8000<br>noisy_input: false | Rasti and Koirala (2022) |
| SUnAA | Sparse Unmixing using Archetypal Analysis | T: 500<br>low_rank: false | T: 500<br>low_rank: false | Rasti et al. (2023) |

*For detailed information on the algorithms and their parameter tuning, please refer to the documentation of the HySUPP package and the corresponding authors in the last column.

To evaluate the accuracy of FVC estimates, we applied regression-based metrics such as Mean Absolute Error (MAE), relative MAE (rMAE), Root Mean Square Error (RMSE), Mean Bias Error (MBE), and the coefficient of determination ($R^2$). MAE was the primary indicator due to its robustness to outliers, while rMAE allowed comparison across scales. All metrics except MBE were computed for both raw predictions and adjusted values obtained after applying an Ordinary Least Squares (OLS) regression to assess linear agreement. For clarity, we denote raw metrics with the subscript *pre* (e.g., $MAE_{pre}$, $R^2_{pre}$) and regression-adjusted metrics with *post* (e.g., $R^2_{post}$). All *pre* metrics were calculated directly between the raw model predictions and the reference values, without applying any regression fitting. Negative $R^2_{pre}$ values indicate that the raw model predictions performed worse than predicting the mean reference FVC, typically due to high variance or systematic bias. MBE was only calculated for raw predictions, as OLS adjustment inherently removes mean bias. This dual evaluation was chosen to ensure both statistical robustness and interpretability, and is further supported by Cooper et al. (2021), who emphasized the importance of including observed vs. predicted comparisons for transparent model assessment. The significance of regression slopes was tested using two-sided t-tests, with *p*-values less than 0.001 considered significant.

# 4 Results

## 4.1 Classification Accuracy of Reference Datasets

The classification results of the UAV-based orthomosaic and the pan-sharpened PNEO image serve as the essential reference foundation for validating the EnMAP-derived FVC estimates. Both datasets were classified independently using an object-based approach, as described in Sect. 3.2.5, and were spatially aligned through prior co-registration procedures.

Classification accuracies for both datasets are summarized in Table 3. The UAV orthomosaic classification achieved high performance for both classes (*Tillandsia*/non-*Tillandsia*), with overall accuracy scores of 0.91 and 0.92 and an F1-score of 0.92. Slightly lower producer's accuracy for the non-*Tillandsia* class suggests minor omission errors. The PNEO classification yielded similarly strong results, with overall accuracy scores of 0.96 and 0.95 and an F1-score of 0.96. Slightly lower user accuracy for the *Tillandsia* class indicates occasional commission errors, likely caused by spectral confusion in shaded or topographically complex areas.

Given that these high-resolution classification results directly underpin the reference dataset used for validating the EnMAP-based unmixing outputs, their accuracy and reliability are essential. The spatial patterns of *Tillandsia* were

**Table 3** Classification accuracy metrics, including overall, user's, producer's accuracy, and F1-score for *Tillandsia* and non-*Tillandsia* classes based on P4 RTK orthomosaic and PNEO data sources. The error matrix and derived metrics provide insight into classification reliability across classes, with F1 scores indicating balanced accuracy performance for each dataset.

| Class | Data Source | User's Accuracy | Producer's Accuracy | Overall Accuracy |
|---|---|---|---|---|
| Non-*Tillandsia* | P4 RTK Orthomosaic | 0.9663 | 0.8687 | 0.9148 |
| *Tillandsia* | P4 RTK Orthomosaic | 0.8829 | 0.9703 | 0.9244 |
| F1-Score | P4 RTK Orthomosaic | *0.9196* | | |
| Non-*Tillandsia* | Pléiades Neo | 0.9798 | 0.9327 | 0.9557 |
| *Tillandsia* | Pléiades Neo | 0.9307 | 0.9792 | 0.9544 |
| F1-Score | Pléiades Neo | *0.9550* | | |

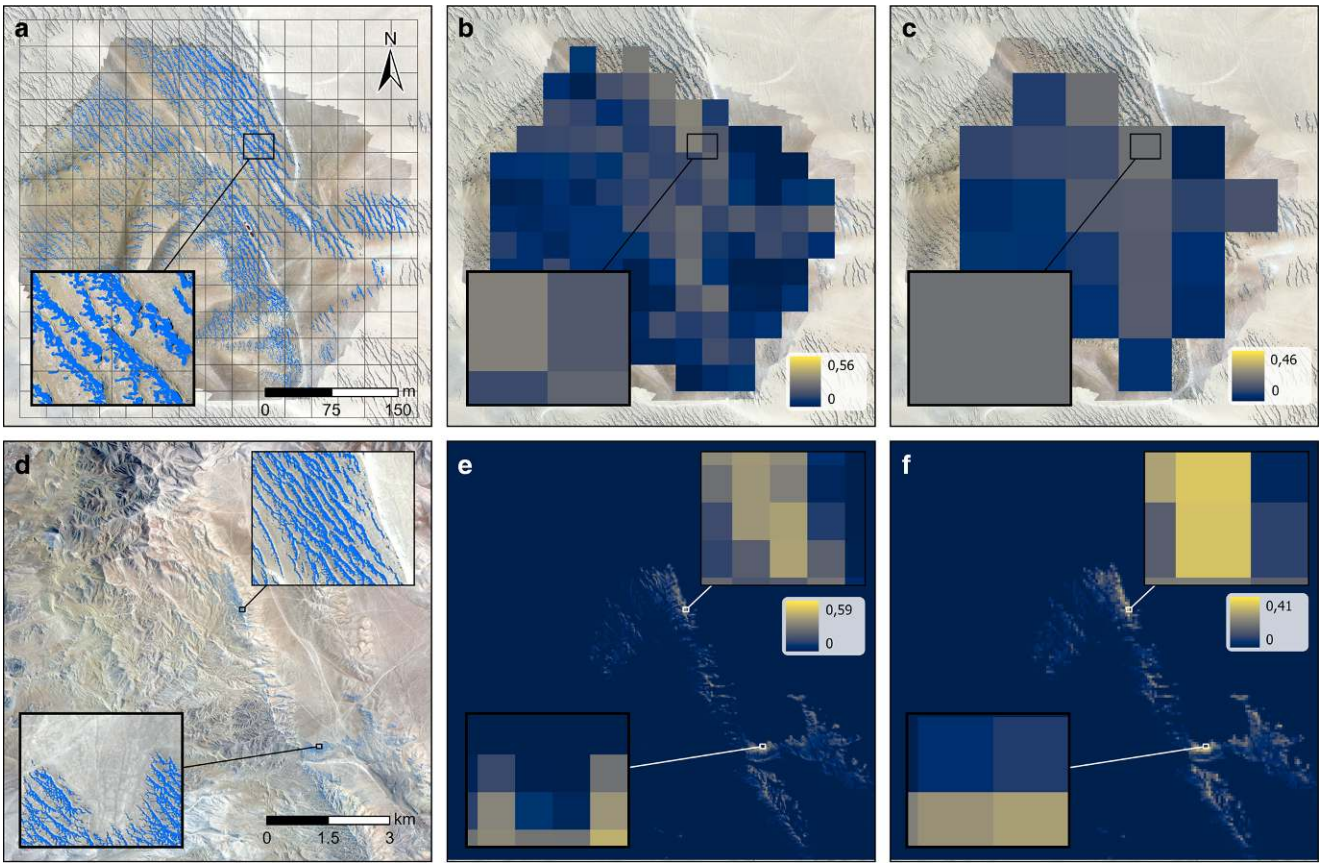


**Fig. 6** Classification results for *Tillandsia* across reference datasets: **a** ultra-high-resolution orthomosaic; **b, c** aggregated to 30 and 60 m using polygon grids and zonal statistics; **d** pan-sharpened PNEO image; **e, f** aggregated to 30 and 60 m using polygon grids and zonal statistics.

clearly captured in both datasets, as shown in Fig. 6. Subplots A and D illustrate the original classifications (blue-colored band structures), while subplots B/C and E/F display the same information aggregated to 30 and 60 m spatial resolution, respectively, using grid-based zonal statistics. To ensure visual comparability between reference and predicted values, the maximum cover fraction in the aggregated reference maps was scaled to match the highest *Tillandsia* abundance predicted by the models.

## 4.2 Results of Local FVC Estimation Using Field-based Spectra

Model accuracy for the local FVC estimates based on the field-based spectral library is shown in Table 4, Table 5 (see Appendix), and Fig. 7 for both 30 and 60 m resolutions. Following the evaluation scheme described in Section 3.4, all metrics are reported in both pre-fitted and post-fitted form. Visual results are provided in Figs. 8 and 9.

Across all local models and both resolutions, $MAE_{pre}$ values varied from 3.1 to 19.6%, with an overall average of 11.1% (Fig. 7). These values quantify the raw predic-

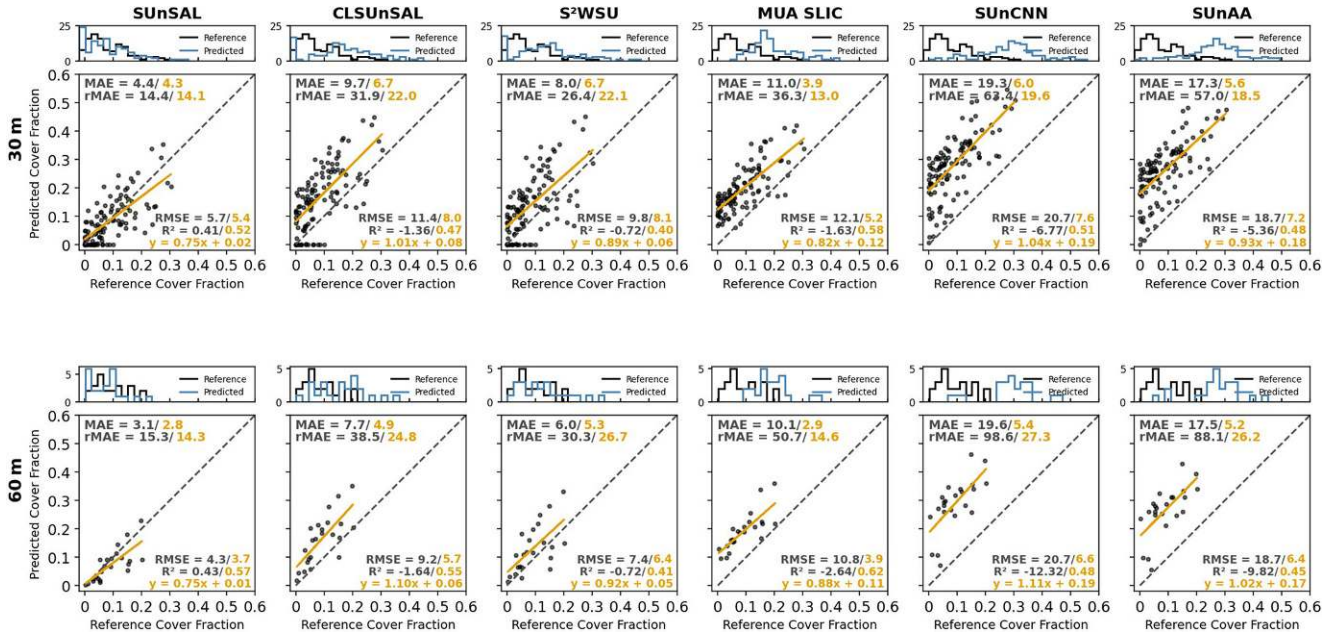


**Fig. 7** Scatter plots of reference (x-axis) versus predicted (y-axis) fractional cover of *Tillandsia* for six unmixing algorithms in the local area. Upper panels show 30 m pixels ($n = 115$); lower panels show aggregated 60 m pixels ($n = 23$). The dashed line marks 1:1 agreement, and the yellow solid line shows the linear regression (OLS) fit. Marginal histograms display the distribution of reference and predicted values for visual comparison

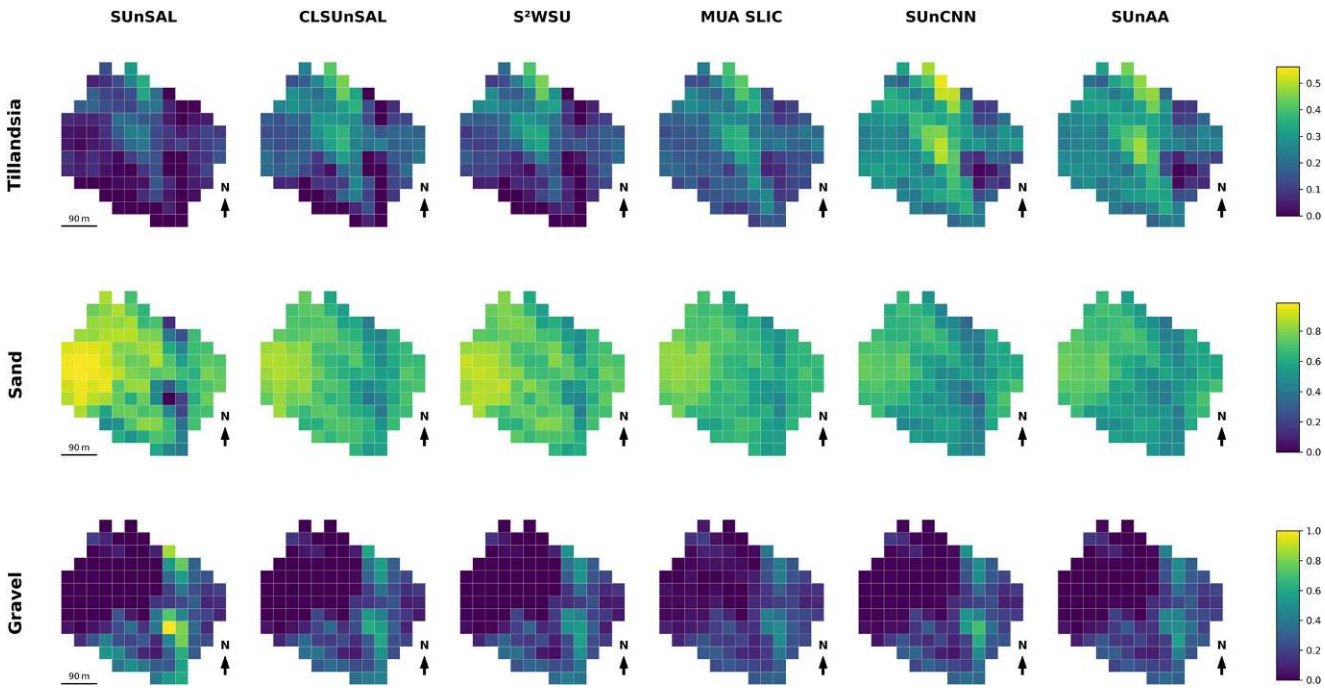


**Fig. 8** Normalized fractional cover maps for the three EMs *Tillandsia*, sand, and gravel (rows), obtained by applying six unmixing algorithms (columns) to the EnMAP image. Only EnMAP grid cells fully covered by the reference orthomosaic were included to ensure conservative validation

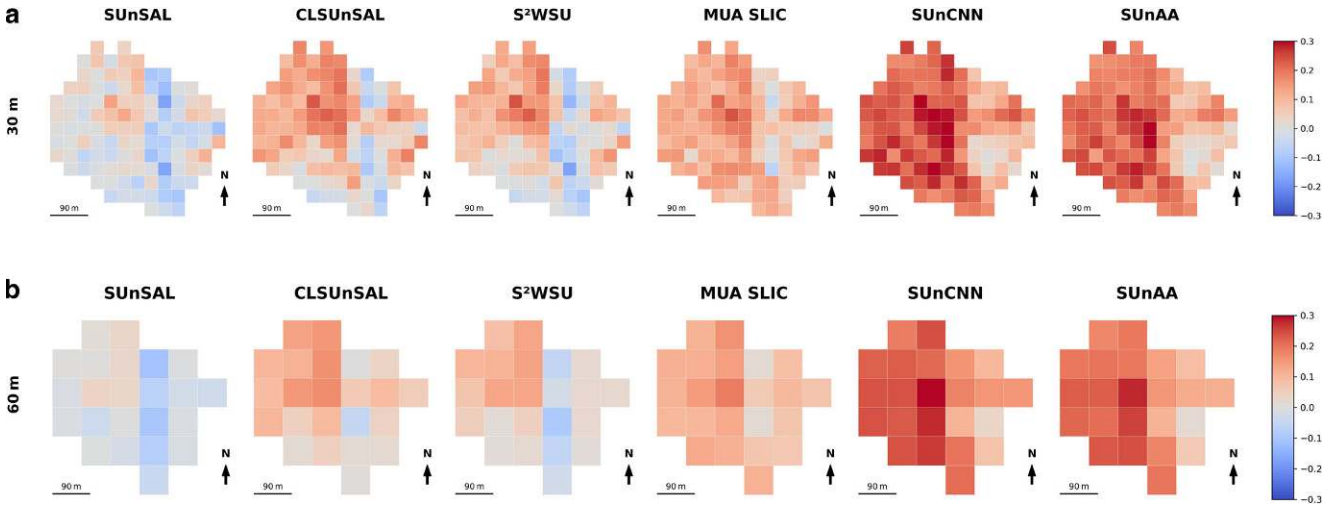


**Fig. 9** Spatial distribution of prediction errors (residuals) in the local area at two spatial resolutions: **a** 30 m and **b** 60 m. Residuals are calculated as the difference between model predictions and reference values (prediction–reference), with red indicating overestimation and blue indicating underestimation

tive accuracy before regression fitting. The corresponding $rMAE_{pre}$ values spanned from 14.4 to 98.6%, highlighting variability in performance across evaluated models and resolutions. MBE indicates an overall trend toward overestimation, ranging from –1.7 to +19.6%, with most models showing a substantial positive bias. Notably, SUnSAL was the only model exhibiting a near-zero bias, slightly underestimating FVC at 30 m resolution.

SUnSAL emerged as the most robust model in terms of raw predictive performance. It achieved the lowest $MAE_{pre}$ values (4.4% at 30 m and 3.1% at 60 m), low $RMSE_{pre}$ values (5.7 and 4.3%, respectively), and an almost negligible bias (MBE = < 1% at 30 m). Unlike models that benefit primarily from post-hoc regression fitting, SUnSAL provided reliable predictions directly from the unmixing process. Although its $R^2_{post}$ values were moderate (0.52 at 30 m and 0.57 at 60 m), they are arguably more meaningful than those of other models, as they reflect explained variance under minimal systematic bias.

In contrast, MUA SLIC performed best after post-fitted regression evaluation. Although its raw predictions were less accurate ($MAE_{pre}$ of 11.0% at 30 m and 10.1% at 60 m, both with substantial positive bias), it achieved the highest $R^2_{post}$ values (0.58 and 0.62) and the lowest $MAE_{post}$ values (3.9 and 2.9%). This indicates that the algorithm effectively reproduces the overall variance structure of the reference data, but lacks precision in its direct predictions.

Among the least accurate models, SUnCNN and SUnAA produced the weakest results. Both models showed severe overestimations (MBE > 17%), negative $R^2_{pre}$ values, and $RMSE_{pre}$ values exceeding 18%, indicating that their apparent $R^2_{post}$ values (approaching 0.5) are driven largely by regression fitting rather than intrinsic predictive power.

Upscaling to 60 m resolution led to performance improvements in most models, primarily through reductions in $MAE_{pre}$ and MBE. This smoothing effect likely results from decreased spatial misalignments and subpixel variability. However, it did not compensate for the structural weaknesses of the poorest-performing models. As shown in Fig. 7, SUnSAL, CLSUnSAL, and $S^2$WSU occasionally failed to capture low FVC values (0 to 10%) in the reference data, resulting in false negatives. In contrast, SUnCNN and SUnAA frequently produced false positives, assigning 10 to 30% FVC to areas without observed *Tillandsia* presence. These tendencies are also reflected in the marginal histograms above the scatter plots, where most models, except SUnSAL, exhibit shifted predicted distributions indicative of systematic overestimation.

These quantitative findings align with the spatial predictions and associated residual patterns visualized in Figs. 8 and 9. The FVC maps in Fig. 8 illustrate the spatial distribution of the three EMs (*Tillandsia*, sand, and gravel) derived from the field-based spectral library across all models at 30 m resolution. While all algorithms successfully capture the general banded structure of *Tillandsia*, the predicted abundance levels vary markedly between models.

The corresponding residual maps in Fig. 9 highlight these discrepancies. SUnSAL shows the fewest over- or underestimations, whereas SUnCNN and SUnAA clearly overpredict FVC across large parts of the scene. In many locations where the reference data indicates no *Tillandsia* presence, these models assign FVC values between 10 and 30%, resulting in widespread false positives.

Overall, SUnSAL stands out as the most reliable model for generating unbiased and directly interpretable predictions, without the need for post-hoc regression evaluation.

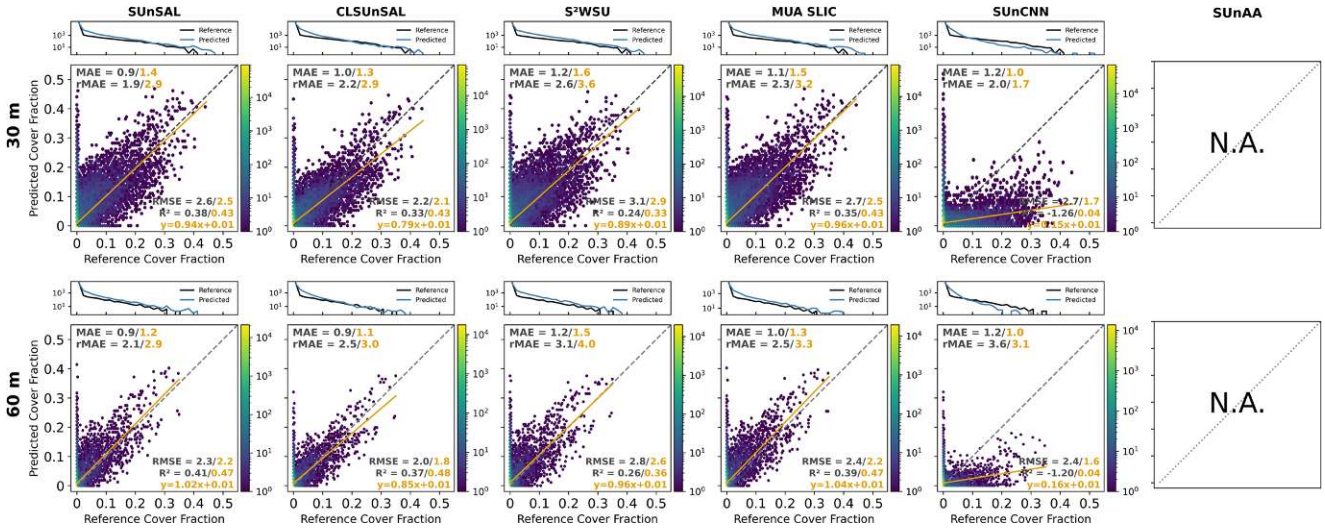


**Fig. 10** Scatter plots of reference (x-axis) versus predicted (y-axis) fractional cover of *Tillandsia* for the six unmixing algorithms in the regional area. Upper panels show 30 m pixels ($n = 120{,}726$); lower panels show the same scene aggregated to 60 m grid cells ($n = 30{,}267$). The grey dashed line denotes perfect 1: 1 agreement, while the solid line is the ordinary-least-squares fit for each algorithm. Marginal histograms placed above every scatter plot depict the frequency distributions of reference (black) and modelled (blue) values, allowing for a visual comparison of value ranges and skewness

By contrast, MUA SLIC demonstrates limited accuracy in its raw outputs but performs well in post-fitted analyses, indicating a strong ability to reproduce overall variance patterns despite lacking precise predictive accuracy.

### 4.3 Results of Regional FVC Estimates Using Image-Based Spectra

In contrast to the unified analysis of the local models, the evaluation of regional models was divided into two parts to account for residual skewness (Fig. 16; see Appendix) and to enable a more targeted interpretation. Section 4.3.1 presents the results based on all EnMAP pixels, while Sect. 4.3.2 focuses on pixels with confirmed *Tillandsia* presence (FVC > 0), where the assumption of normality was restored (Fig. 17; see Appendix). This separation allows for both a scene-wide assessment of detection capacity and a focused evaluation of model accuracy in vegetated areas.

#### 4.3.1 Regional Model Results Assessment Including All Reference Values

An overview of model accuracy metrics for the regional models, based on the image-based spectral library and using all pixels from the EnMAP scene, is presented in Table 6, Table 7 (see Appendix), and the scatterplots in Fig. 10 for both 30 and 60 m resolutions.

Across all regional models and both resolutions (excluding SUnCNN and SUnAA due to poor or invalid results), the $MAE_{pre}$ ranged from 0.9 to 1.2%, with an overall average of 1.0%. The corresponding $rMAE_{pre}$ varied between 1.9 and 3.1%. The MBE was near zero for all models, demonstrating the absence of systematic over- or underestimation in the raw predictions. However, the $R^2_{pre}$ values remained low to moderate, with the best-performing models (SUnSAL, CLSUnSAL, and MUA SLIC) reaching values between 0.33 and 0.41 across both resolutions. This indicates that, despite low absolute errors, the models explained only a limited portion of the variance in the reference data. This is likely due to the strong class imbalance in the scene, where the majority of pixels exhibit zero vegetation cover, thus constraining the overall variance that can be captured by the models.

In terms of raw performance (i.e., prediction vs. reference), SUnSAL achieved the best results, with the lowest $MAE_{pre}$ values (0.9% at both 30 and 60 m) and the lowest $rMAE_{pre}$ values (1.9 and 2.1%). CLSUnSAL followed closely ($MAE_{pre}$: 1.0 and 0.9%; $rMAE_{pre}$: 2.2 and 2.5%), while MUA SLIC showed $MAE_{pre}$ values of 1.1 and 1.0% ($rMAE_{pre}$: 2.3 and 2.5%), and $S^2$WSU reached 1.2% at both resolutions ($rMAE_{pre}$: 2.6 and 3.1%). $RMSE_{pre}$ values ranged from 2.0 to 3.1% across all models, with the lowest errors observed for CLSUnSAL (2.2% at 30 m and 2.0% at 60 m).

After applying a linear regression fit, the $R^2_{post}$ values increased noticeably, reaching values between 0.43 and 0.48 for the best-performing models (SUnSAL, CLSUnSAL, and MUA SLIC). This improvement reflects a stronger linear association with the reference data. However, these gains did not correspond to improved predictive accuracy:

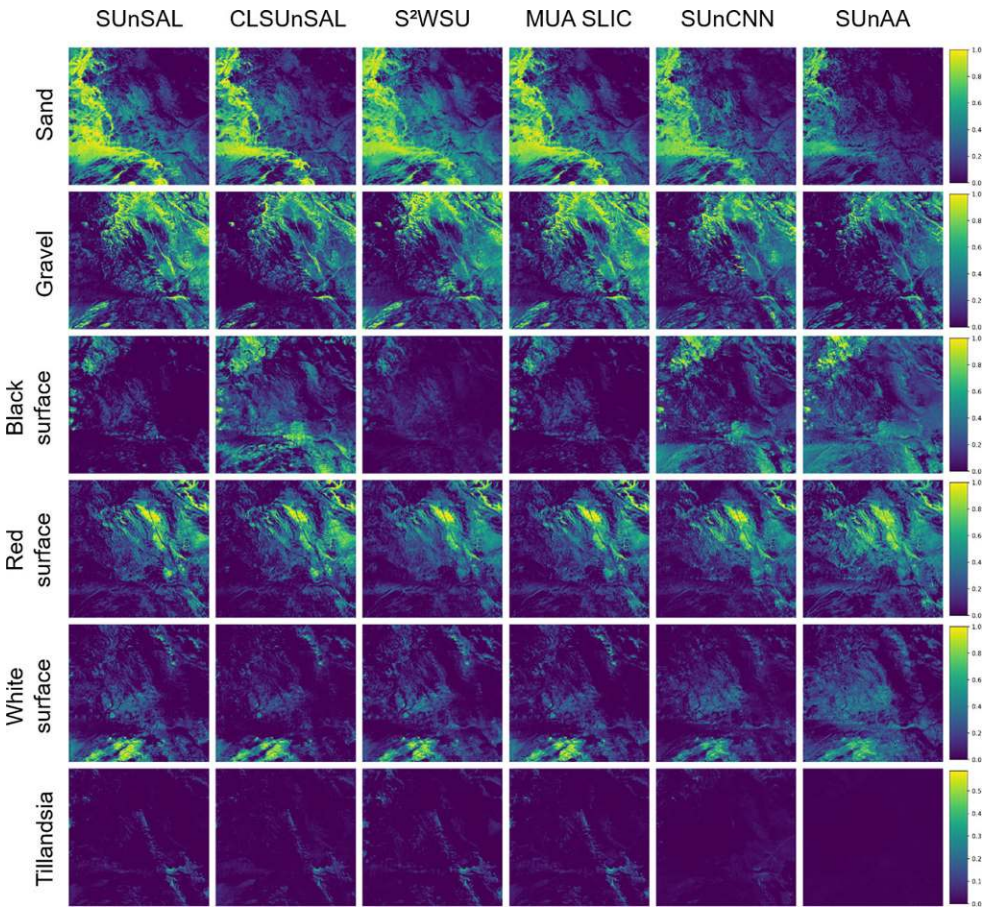


**Fig. 11** Fractional vegetation cover (FVC) of all six EMs (rows) on the regional scale for all sparse spectral unmixing algorithms (columns)

while $RMSE_{post}$ values decreased slightly, both $MAE_{post}$ and $rMAE_{post}$ increased.

Among all models, SUnSAL and CLSUnSAL demonstrated the most balanced performance across evaluation modes (pre- and post-fitted) and spatial resolutions. SUnSAL achieved the lowest $MAE_{pre}$ values (0.9% at both 30 and 60 m) and maintained low $RMSE_{pre}$ values (2.6 and 2.3%), with negligible bias and $R^2_{post}$ values of 0.43 and 0.47. CLSUnSAL performed similarly, with $MAE_{pre}$ values of 1.0 and 0.9%, $RMSE_{pre}$ values of 2.2 and 2.0%, and the highest $R^2_{post}$ value of 0.48 at 60 m resolution.

Visual interpretation of fraction patterns in Fig. 11 reveal a high degree of agreement with the PNEO classification (Fig. 6e). The spatial distribution of the EMs (sand, gravel, red and white surface) was consistent across SUnSAL, CLSUnSAL, $S^2$WSU, and MUA SLIC, with notable differences only for the black surface in certain areas. For *Tillandsia*, the best-performing models produced similar spatial patterns, with most false positives occurring in the northwestern, northeastern, and southwestern parts of the scene (Fig. 12). In contrast, the central region showed slight underestimation of *Tillandsia* cover, despite confirmed presence in the reference data.

To account for the dominance of zero-reference pixels in the full-scene analysis, the following section presents a separate regression using only pixels with FVC > 0 to evaluate model performance in confirmed *Tillandsia* areas.

#### 4.3.2 Fractional Cover Estimation in Confirmed *Tillandsia* Areas

An overview of model accuracy metrics for the regional models, based on the image-based spectral library and restricted to EnMAP pixels with FVC > 0, is provided in Table 8 and Table 9 (see Appendix). The corresponding scatterplots are shown in Fig. 13 for both 30 and 60 m resolutions.

Across all regional models and both spatial resolutions, the average $MAE_{pre}$ after masking was 3%, with individual values ranging from 1.8 to 3.7%. The corresponding $RMSE_{pre}$ averaged 4.6%, spanning from 4.0 to 5.5%. Relative errors ($rMAE_{pre}$) ranged from 4.7 to 8.0%, and $R^2_{pre}$ values improved substantially compared to the full-scene results, reaching up to 0.72 ($R^2_{post}$) in the best case. These results indicate a notable gain in interpretability and consistency across models, with reduced prediction variability and improved statistical fit after masking.

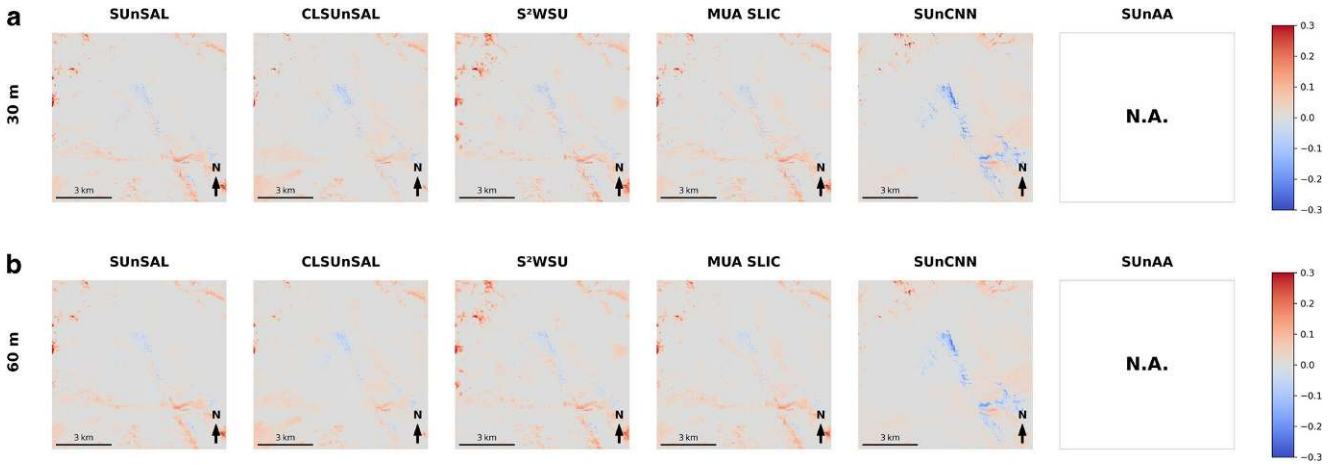


**Fig. 12** Spatial distribution of prediction errors (residuals) in the regional area at two spatial resolutions: **a** 30 m and **b** 60 m. Residuals are calculated as the difference between model predictions and reference values of FVC (prediction–reference). Positive values (red) indicate overestimation; negative values (blue) indicate underestimation. Due to a failure, the results of SUnAA are not shown

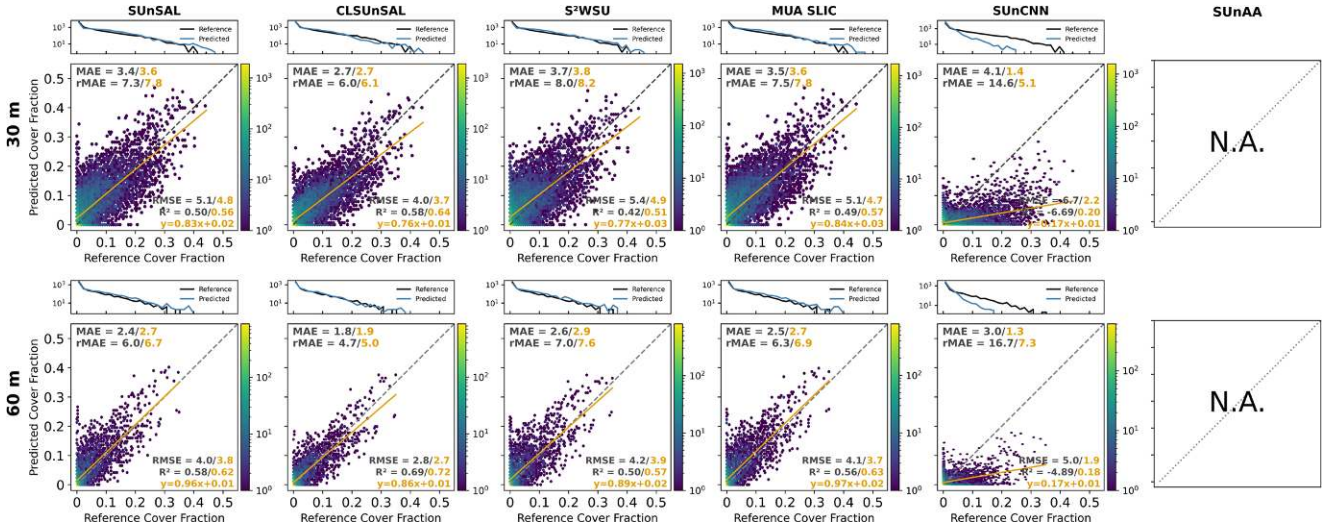


**Fig. 13** Scatter plots of reference (x-axis) versus predicted (y-axis) fractional cover of *Tillandsia* for the six unmixing algorithms in the regional area. Only pixels with confirmed presence of *Tillandsia* (i.e., reference cover > 0) were included. Upper panels show 30 m pixels ($n = 9{,}912$); lower panels show the same scene aggregated to 60 m grid cells ($n = 3{,}617$). The grey dashed line denotes perfect 1: 1 agreement, while the solid line is the ordinary-least-squares fit for each algorithm. Marginal histograms placed above every scatter plot depict the frequency distributions of reference (black) and modelled (blue) values, allowing for a visual comparison of value ranges and skewness

CLSUnSAL achieved the best overall performance, with the lowest $MAE_{pre}$ values (2.7% at 30 m and 1.8% at 60 m), minimal $rMAE_{pre}$ (6.0 and 4.7%), and $RMSE_{pre}$ values of 4.0 and 2.8%, respectively. The model exhibited no systematic bias and the highest $R^2_{post}$ values of 0.64 (30 m) and 0.72 (60 m), confirming its high predictive stability and linear consistency. These results highlight CLSUnSAL as the most balanced and accurate model for estimating the fractional cover of *Tillandsia* under masked conditions.

The second-best performer was SUnSAL, with slightly higher $MAE_{pre}$ values (3.4 and 2.4%), $rMAE_{pre}$ between 7.3 and 6.0%, and strong $R^2_{post}$ values of 0.56 and 0.62. Although it showed minor over- and underestimation tendencies (MBE = 0.01), its predictions were generally reliable across both spatial resolutions. MUA SLIC and S²WSU followed closely, each with $MAE_{pre}$ values of around 3.5 to 3.7% at 30 m and 2.5 to 2.6% at 60 m. While their absolute errors remained competitive, both models showed higher $rMAE_{pre}$ values (up to 8.0%) and slightly lower $R^2_{post}$ values, suggesting less consistent scaling performance, especially in higher FVC ranges.

By contrast, SUnCNN performed poorly in terms of raw prediction accuracy, with the highest $MAE_{pre}$ values (4.1 and 3.0%) and extreme $rMAE_{pre}$ values of up to 16.5%. Despite achieving surprisingly low $MAE_{post}$ values after regression adjustment (1.4 and 1.3%), the corresponding $R^2_{pre}$

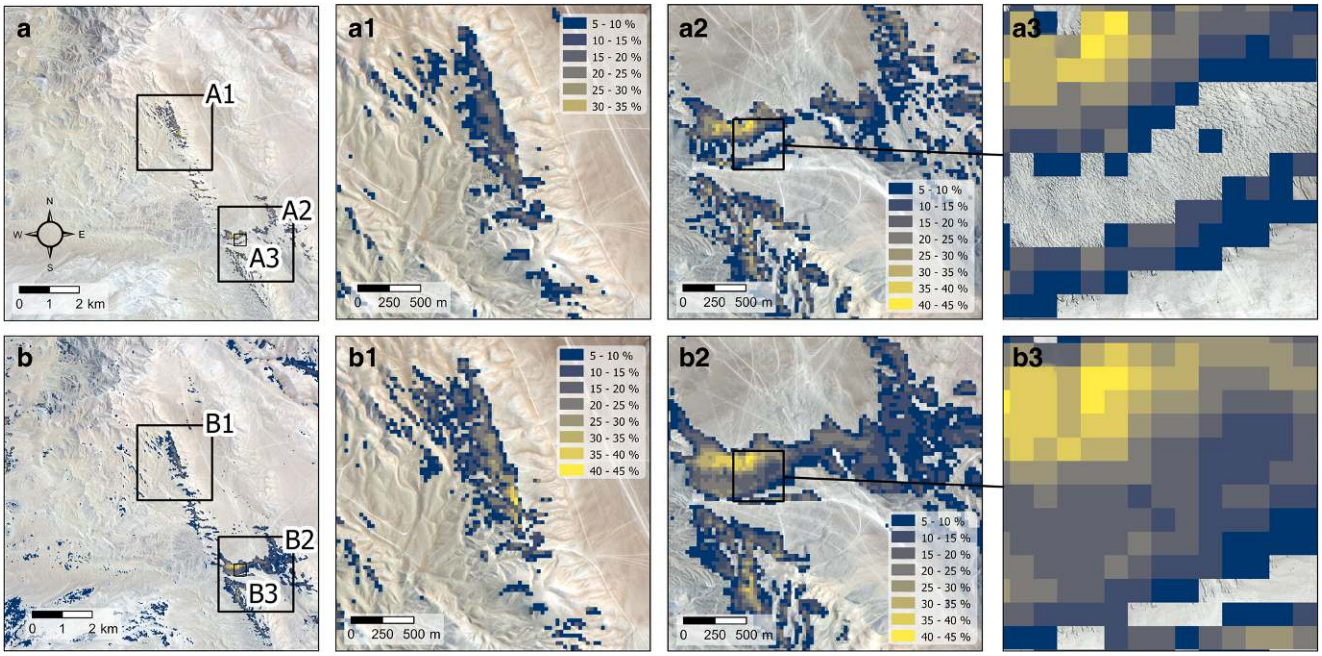


**Fig. 14** Comparison of the fractional cover of *Tillandsia landbeckii* based on the classification of the pan-sharpened PNEO scene (**a**) and the unmixing of the EnMAP scene using the CLSUnSAL algorithm (**b**). Subset images (A1–A3 and B1–B3) offer a more detailed comparison of spatial patterns and classification discrepancies at 30 m resolution

values remained strongly negative (–6.69 and –4.89), reflecting a lack of agreement with the reference data before correction. SUnAA completely failed to estimate FVC and was excluded from analysis. Overall, most models benefited from spatial aggregation, with improved performance at 60 m resolution in nearly all metrics.

To further illustrate the spatial plausibility of the CLSUnSAL predictions, Fig. 14 presents a visual comparison between the EnMAP-derived FVC and the reference FVC based on the classification of the pan-sharpened PNEO scene.

While panel A shows the FVC derived from an object-based classification of PNEO data, panel B displays the unmixing-based results obtained from EnMAP using the CLSUnSAL algorithm. Overall, the spatial patterns of *Tillandsia* are broadly consistent across both datasets. However, localized differences are clearly visible in the subset images (A1–A3 and B1–B3). In panel B1, the EnMAP-derived FVC appears slightly overestimated in the central vegetated band relative to the PNEO-based reference. Conversely, panel A2 shows a fragmented spatial pattern that contrasts with the more continuous distribution in B2. In panel A3, a gap in the classification corresponds to a clearly defined patch in the EnMAP result (B3), suggesting that *Tillandsia* was either missed by the object-based classification or occurred below the 5% threshold applied during reference generation. These differences may also reflect local mismatches in georeferencing, subpixel mixing effects, or uncertainties in the spectral separation of bright surfaces and vegetation.

## 5 Discussion

This study set out to evaluate the potential of EnMAP hyperspectral imagery for detecting and quantifying the fractional vegetation cover of *Tillandsia landbeckii* in the hyper-arid Atacama Desert. As a key structural variable, FVC provides crucial insights into vegetation productivity, physiological condition, and response to environmental change (Liang and Wang 2020), particularly in water-limited ecosystems such as those dominated by tillandsiales.

*Tillandsia* has long posed a challenge for satellite-based remote sensing due to its spectral similarity to bare ground, absence of characteristic chlorophyll absorption features in the visible and near-infrared spectrum, and low fractional cover. Based on these constraints, we have considered *Tillandsia* effectively "invisible" to multispectral satellite sensors. To overcome this limitation, we applied multiple sparse spectral unmixing algorithms and explored the results of two distinct spectral libraries respective to their individual modeling context: a field-based library derived from in situ spectroradiometer measurements and an image-based library extracted directly from the EnMAP scene. These libraries were designed to accommodate different spectral conditions and to explore their respective suitability for FVC estimation in local and regional modeling scenar-

ios. Validation was supported by a high-resolution reference dataset designed to enable consistent, multi-scale comparison of subpixel vegetation estimates.

While the performance of individual algorithms varied, the overall findings underscore the effectiveness of sparse spectral unmixing on hyperspectral EnMAP scenes for detecting *Tillandsia* and estimating its fractional vegetation cover. The following subsections discuss the influence of different spectral libraries, identify key limitations, explore opportunities for improvement, and reflect on broader implications for remote sensing of low-signal vegetation in dryland ecosystems.

### 5.1 Field-Based Spectral Library for FVC Estimation

Among all algorithms tested, SUnSAL delivered the most accurate raw predictions, with a $MAE_{pre}$ of 4.4% and a $R^2_{pre}$ of 0.41 at 30 m resolution. After aggregating to 60 m pixel resolution, the performance improved further ($MAE_{pre}$ = 3.1%, $R^2_{pre}$ = 0.43), which we attribute primarily to the smoothing effect of spatial aggregation outlined in Sect. 3.2.5. By increasing the grid cell size, spatial mismatches and subpixel variability were reduced, thereby enhancing agreement with the reference data. This finding aligns with earlier studies that showed how coarser resolutions can help mitigate co-registration errors and spatial uncertainties in validation datasets (e.g., Cooper et al. 2021; Juola et al. 2024; Schwieder et al. 2014).

However, most local models exhibited a systematic tendency to overestimate the FVC of *Tillandsia*. This was reflected in consistently positive mean bias errors (MBE = 3.9 to 19.6%) across nearly all models and negative $R^2_{pre}$ values, indicating a fundamental mismatch between predictions and reference data, as outlined in Section 3.4. These biases contributed to inflated error metrics, particularly in models with larger overall deviations. One likely explanation for this systematic overestimation lies in the combination of low fractional abundance and the nature of the spectral library used for unmixing. Although *Tillandsia*'s characteristic absorption features, especially in the SWIR domain, likely enabled its distinction from other EMs, its actual contribution to the pixel-level reflectance was often marginal compared to dominant surfaces such as sand or gravel. These materials exhibit higher overall reflectance than *Tillandsia* (see Fig. 5), which likely suppresses its apparent spectral signal and amplifies overestimation in the abundance retrieval. This interpretation is consistent with previous findings from sparsely vegetated environments (e.g., Cooper et al. 2021; Schwieder et al. 2014), particularly in cases involving low-biomass shrubs, and aligns with the growth form of *Tillandsia*, which typically occurs in narrow bands only 30–60 cm in height, 20–40 cm in width, and 2–4 m in length (Rundel et al. 1997).

Beyond the influence of low fractional abundance, a second potential explanation for the observed overestimation relates to the nature of the field-based spectral library. While our in situ measurements provided spectrally pure EMs under controlled conditions (see Sect. 3.2.1), they may not have adequately captured the variability and sensor-specific characteristics present in the EnMAP scene. Notable discrepancies, for instance, in the sand EM spectrum, suggest that the mismatch between field and image conditions introduced scaling inconsistencies during the unmixing process. In such cases, the field-based spectra may reflect conditions not represented in the satellite scene, thereby introducing systematic errors into the unmixing output (Borsoi et al. 2021). Furthermore, the EnMAP scene was acquired approximately one year after the field campaign, although it was during the same seasonal period. While phenological dynamics in *Tillandsia* are assumed to be relatively stable and not subject to significant short-term variation, interannual differences in soil moisture, atmospheric properties, or illumination conditions may nonetheless have affected the spectral signal of both vegetation and background surfaces. This temporal gap introduces an additional layer of uncertainty and exemplifies the broader challenge of applying externally acquired spectral libraries to satellite data, especially when environmental or sensor conditions differ (Borsoi et al. 2021).

Notably, several models showed substantial improvement after post-fitting, suggesting that much of the bias in raw predictions was systematic rather than random. This highlights the potential for enhancing accuracy through improved spectral matching, internal consistency between image and EM characteristics, or refined algorithm tuning, rather than relying solely on statistical correction. This is exemplified by the MUA SLIC model, which achieved stronger post-fitted performance ($MAE_{post}$ = 3.9 to 2.9%; $R^2_{post}$ = 0.58 to 0.62) despite poor raw predictions. In this case, the substantial bias (MBE = 10.1 to 10.8%) could likely have been mitigated through better spectral alignment or model design, resulting in lower $MAE_{pre}$ values without post hoc adjustment.

Despite these limitations in raw prediction accuracy, several models nonetheless reproduced the spatial patterns of *Tillandsia* abundance reasonably well. Two factors likely contributed to this: first, the limited spectral diversity within the local study area allowed for stable unmixing using a compact spectral library with only three EMs. This aligns with the principle of minimizing EM complexity to enhance numerical stability in linear unmixing models (Adams and Gillespie 2006). Prior field knowledge further supported the accurate identification of ground materials and reduced spectral ambiguity. Second, the high spectral resolution of EnMAP, particularly in the SWIR domain between 1000 and 2450 nm, was likely critical for distinguishing *Tilland-*

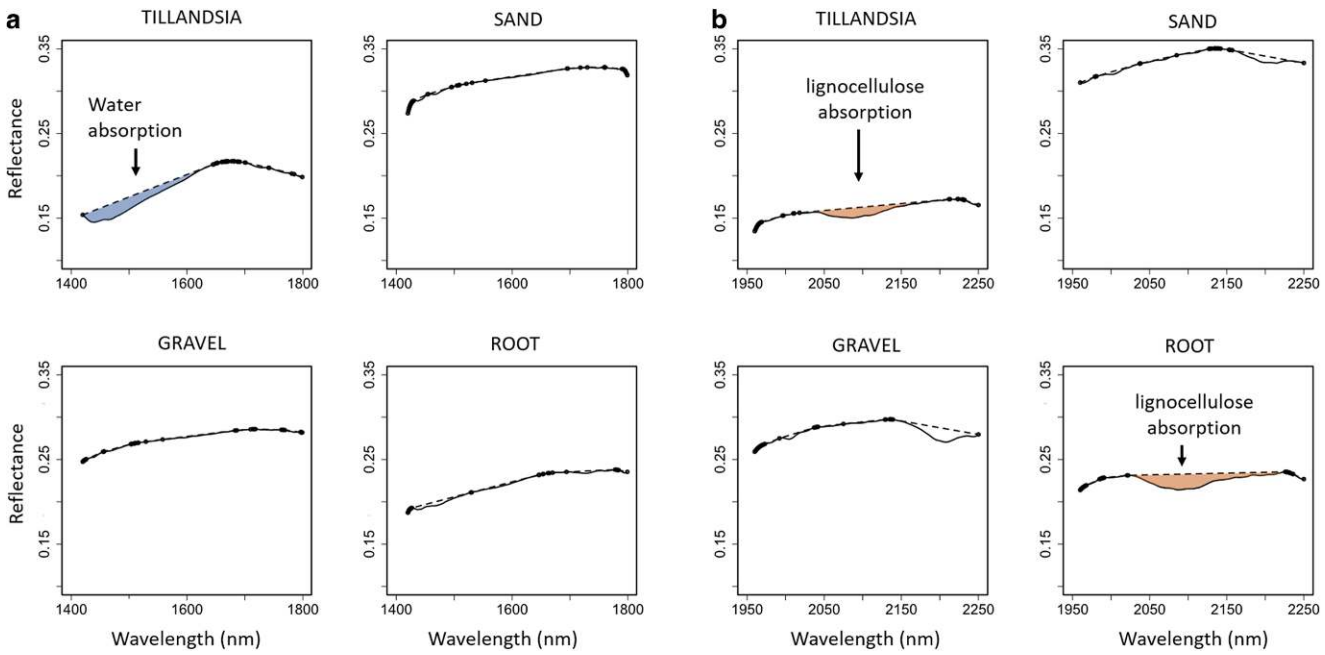


**Fig. 15** Convex Hulls representing the two most significant absorption features of *Tillandsia* compared to the background EM after continuum removal. The convex hulls represent the upper envelope of spectral data created by connecting local maxima with straight-line segments. This geometric construct normalizes reflectance spectra, allowing for a clearer comparison of absorption features. By isolating key absorption bands in the *Tillandsia* spectrum, the convex hull highlights the distinctiveness of its spectrum compared to other EMs. Panel **a** highlights the 1400–1800 nm range, sensitive to lignin, water, starch, and sugar, while Panel **b** focuses on the 2000–2200 nm range, prominently associated with lignin and cellulose. Spectra were obtained using an ASD FieldSpec 4

*sia* from spectrally similar substrates. Unlike multispectral sensors, which lack the resolution to capture narrow absorption features, EnMAP provides dense spectral sampling and captures subtle features related to vegetation constituents such as water and lignocellulose (Asner and Heidebrecht 2002; Dennison et al. 2019; Guerschman et al. 2009), thereby enhancing the detection of both photosynthetic and non-photosynthetic vegetation. In our view, this capability was essential for discriminating low-signal *Tillandsia* vegetation in a setting where the plant often contributes only marginally to the overall pixel reflectance.

Although not the central focus of this study, an exploratory analysis of the collected field spectra based on convex hull normalization provided important support for our interpretation. It confirmed the presence of distinct SWIR absorption features in *Tillandsia*, including a pronounced water absorption signal at ∼1450 nm and a lignocellulose peak around ∼2090 nm (Fig. 15), features not observed in the other EMs. The water absorption feature is particularly noteworthy, as *Tillandsia* may be one of the few vegetation types exhibiting such a signal in the hyper-arid Atacama Desert (Pinto et al. 2006; Rundel et al. 1997). However, some of these informative spectral regions (e.g., 895–982 nm and 1294–1472 nm) were excluded from the unmixing process due to known artifacts in the EnMAP scene (Sect. 3.3.2). Retaining these bands through improved atmospheric correction in future analyses may enhance unmixing accuracy. The lignocellulose absorption feature, indicative of dry or non-photosynthetic plant tissue (Verrelst et al. 2023), was clearly present in the *Tillandsia* EM spectrum (Fig. 15b) and was reliably captured by EnMAP. This is particularly relevant because, despite its ability to photosynthesize, *Tillandsia* lacks the characteristic spectral signatures of green vegetation, such as the green reflectance peak, red chlorophyll absorption, and red-edge slope (see Sect. 1). As a result, traditional multispectral sensors have failed to detect the species reliably in previous studies (e.g., Mikulane et al. 2022; Wolf et al. 2016), primarily due to their spectral limitations in the VIS/NIR domain.

While we did not empirically evaluate Sentinel-2 or Landsat-8/9 for mapping *Tillandsia*, we assume that these features are likely only partially captured by the broad SWIR bands of these multispectral systems, which typically offer just two wide bands (e.g., ∼1610 nm and ∼2190 nm) with bandwidths of 90–180 nm (European Space Agency ESA; U.S. Geological Survey USGS). Such coarse sampling may obscure narrow absorption features, effectively diminishing the separability of *Tillandsia* from background substrates. EnMAP, on the other hand, provides a spectral sampling interval of ∼10 nm, enabling the detection of these subtle reflectance changes. While these initial findings are promising, further quantitative analyses are needed to confirm the specific role of these absorption features in improving FVC estimates and species-level de-

tection of *Tillandsia*, particularly in light of their potential to overcome the limitations of conventional multispectral approaches.

These findings support a broader insight into the limitations of using externally acquired EM in image-based spectral unmixing. While field-based spectra offer high spectral fidelity and are typically regarded as physically pure, their application to satellite data can be impaired by differences in atmospheric conditions, illumination, and sensor characteristics. This observation aligns with previous studies emphasizing the limited transferability of *ex situ* spectral libraries in the presence of spectral variability (Borsoi et al. 2021). To address these limitations, we complemented the local analysis with a second, image-based spectral library tailored to the characteristics of the EnMAP scene. This dual-library approach enabled a structured comparison between externally measured and scene-derived endmembers, which is examined in the following section.

### 5.2 Image-based Spectral Library for FVC Estimation

The regional-scale regression metrics appear favorable, but closer inspection reveals several statistical limitations. As presented in Sect. 4.3.1, the regional models yielded relatively low absolute errors across the full EnMAP scene, with $MAE_{pre}$ values below 1.2% and negligible mean bias. However, these seemingly strong metrics must be interpreted with caution due to substantial class imbalance in the dataset. The vast majority of pixels in the reference data contain no *Tillandsia*, resulting in a heavily zero-inflated distribution. This disproportionate frequency of background pixels affects the overall variance structure and biases the residual distribution, thereby distorting regression metrics such as $MAE_{pre}$, $RMSE_{pre}$, and $R^2_{pre}$. Moreover, many FVC values cluster around very low percentages (<5%), as seen in the scatterplots (Fig. 10). In the low-FVC range, even moderate overestimations contribute little to global error metrics, potentially masking larger errors in ecologically relevant areas with non-zero *Tillandsia* cover.

This distortion is confirmed by the residual histograms (Fig. 16; see Appendix), which reveal a skewed and heteroscedastic error distribution. Such characteristics indicate violations of key assumptions of linear regression, most notably the normality and homoscedasticity of residuals (Gelman and Hill 2007; Knief and Forstmeier 2021), which are not met in our case. A particularly striking example is the frequent prediction of positive *Tillandsia* cover in pixels where the reference indicates complete absence (FVC = 0), resulting in a characteristic "string-of-pearls" pattern in the scatterplots (Fig. 10), where predicted values cluster vertically along the y-axis. These false positives are not randomly distributed but show clear spatial patterns, particularly in the northwestern, northeastern, and southwestern parts of the EnMAP scene (Figs. 11 and 12). A likely explanation lies in spectral confusion, where the models may misinterpret mixed signals from dark surfaces or shaded areas as the weak and often ambiguous spectral features of *Tillandsia*, a problem already noted in earlier studies involving shadowed terrain (Mikulane et al. 2022). This confusion may be further amplified by limitations in the spectral library, particularly at the regional scale, where the number and diversity of surface materials increase.

Therefore, a key challenge lies in the ability of the spectral library to adequately represent the wide range of surfaces present in the EnMAP imagery. Its composition and completeness critically affect model reliability, as insufficient representation of spectral diversity can lead to systematic misclassification and degraded unmixing performance. In our case, EMs were manually extracted based on visual interpretation of color and topographic uniformity, using the PNEO image as a high-resolution reference. While this approach is generally considered robust (Borsoi et al. 2021) and accounts for spectral variability to some extent, it may not fully capture all relevant surface types, particularly those that are less prominent or spatially heterogeneous (Pervin et al. 2022). These limitations are especially relevant for algorithms like SUnAA, which assume that all materials of interest can be expressed as convex combinations of known EMs (Rasti et al. 2023). While this assumption held at the local scale, where the set of EMs was well defined and limited to three classes, it likely broke down at the regional level, where spectral variability and unknown surface types increased. This mismatch could explain why SUnAA performed, albeit with notable overestimation, at the local level but failed to generalize regionally. Expanding the spectral library, especially by incorporating less obvious or spectrally complex EMs, therefore represents a promising path forward. A more comprehensive and representative library may help reduce false positives, improve material separability, and ultimately strengthen unmixing performance at larger spatial scales. To support this goal, future studies could complement manual EM selection with automated or semi-automated EM extraction techniques. Approaches such as the Pixel Purity Index (PPI), N-FINDER, or Iterative Error Analysis (IEA) have proven useful for identifying spectrally pure pixels in complex scenes and could help reduce subjectivity in library construction (Chakravortty 2024; Plaza et al. 2011, 2002). While fully automated methods remain challenging in natural, heterogeneous environments (Kale et al. 2019; Keshava and Mustard 2002; Plaza et al. 2012), integrating algorithmic tools with expert knowledge may improve reproducibility and increase the likelihood of capturing spectrally subtle or spatially limited surface types. In this way, spectral libraries can be made more robust and transferable.

### 5.3 FVC Estimation in Confirmed *Tillandsia* Areas

To address the statistical limitations outlined in Sect. 5.2 and to assess model performance under ecologically meaningful conditions, we conducted a second regression analysis using only pixels with confirmed *Tillandsia* presence (i.e., reference FVC > 0; see Sect. 4.3.2) and subplots A1/B1 and A2/B2 in Fig. 14. This targeted evaluation reduced the influence of the dominant zero class, restored key regression assumptions, most notably, residual normality and homoscedasticity, and enhanced the interpretability of the regional model results. By focusing on the vegetated portion of the EnMAP scene, we could more directly assess each model's ability to estimate FVC across the actual range of observed *Tillandsia* cover (Fig. 6e, f), rather than evaluating their ability to predict absence. As discussed earlier, most models incorrectly predicted *Tillandsia* cover for pixels that were classified as bare ground in the reference data, leading to systematic false positives in specific areas of the scene. This misclassification likely stemmed from an insufficient number and diversity of EMs in the spectral library, which failed to represent the full spectral heterogeneity of the region.

By leveraging our high-resolution reference dataset and excluding misclassified pixels from the evaluation, the masked analysis removed a major source of spectral confusion and enabled a more ecologically meaningful assessment of model performance in FVC estimation. It revealed the actual predictive power of the unmixing models in areas with confirmed *Tillandsia* presence. We successfully identified the core distribution zones of *Tillandsia* and explained 58% of the variance in the reference FVC (prediction vs. reference) and 64% after linear regression adjustment at 30 m resolution (MAE = 2.7). At 60 m resolution, the models explained even up to 72% of the variance (OLS regression vs. reference), with a corresponding $MAE_{post}$ of 1.9%. While these MAE values are slightly higher than those from the unmasked analysis, they are no longer distorted by zero-inflation and thus provide a more realistic and ecologically valid measure of model accuracy. Comparable MAE values have been reported by Cooper et al. (2021), who observed that classification accuracies were highest when distinguishing between vegetation and non-vegetation, and emphasized that such results are consistent with other studies applying hyperspectral data to estimate FVC (e.g., Dennison et al. (2019)). This supports our interpretation that the spectral contrast between *Tillandsia* and bare ground is sufficiently strong to be captured by hyperspectral sensors, enabling FVC estimates of promising accuracy, provided that validation is carried out under ecologically meaningful conditions.

This achievement becomes particularly evident when visually comparing the *Tillandsia* distribution pattern from our reference data (Fig. 6e) with the model results in Figs. 11 and 14. The (un)covered area of *Tillandsia* is clearly captured by the models CLSUnSAL, SUnSAL, $S^2$WSU, and MUA SLIC, where its characteristic spatial spread also matches the *Tillandsia* field classified earlier by Mikulane et al. (2022). Although subplot A3 of Fig. 14 shows an apparent gap in the classified reference map, caused by the applied visualization threshold omitting reference FVC values below 5%, the overall spatial pattern remains highly consistent. The corresponding predictions in subplot B3 indicate low but non-zero cover, reinforcing the notion that the models slightly overestimate FVC in the lower range rather than the reference, omitting actual vegetation. Despite minor local discrepancies, the spatial consistency between the EnMAP-based predictions and the high-resolution PNEO reference supports the reliability of our model outputs. While most of these differences likely stem from subpixel mixing or minor classification uncertainties, small spatial mismatches between the EnMAP scene and the reference data cannot be entirely excluded. Although the alignment appeared visually consistent and was supported by zonal aggregation, the spline-based co-registration lacked quantitative accuracy metrics such as RMSE, and the use of *Tillandsia* patches as control points may have introduced slight positional uncertainties, particularly in shaded or topographically complex areas.

The findings presented in this study demonstrate that even a plant long considered "invisible" to satellite remote sensing, due to its low spectral contrast, lack of chlorophyll absorption, and sparse spatial structure, can be made visible through the use of high-resolution hyperspectral data and sparse spectral unmixing. Remarkably, this was achieved using only spectral information, without relying on structural, morphological, or contextual features. Based on a deliberately small and interpretable spectral library, we could estimate both the spatial distribution and FVC of *Tillandsia landbeckii* across regional scales. This is a crucial step toward quantifying vegetation abundance in extreme environments, highlighting the potential of spectral unmixing to derive ecologically meaningful variables in data-scarce regions. Since FVC is a key input for estimating aboveground biomass and understanding the dynamics of vegetation, our results pave the way for large-scale assessments of *Tillandsia* FVC estimates and their role in fog-dependent ecosystems of the Atacama Desert.

## 6 Conclusion

This study demonstrates, for the first time, that the fog-dependent species *Tillandsia landbeckii*, long considered undetectable by multispectral satellite sensors, can be reliably identified and quantified using spaceborne hyperspec-

tral imagery. By applying semi-supervised sparse spectral unmixing to EnMAP data, we estimated the subpixel fractional vegetation cover (FVC) of *Tillandsia* solely based on spectral information, thereby overcoming key limitations of conventional classification approaches on multispectral satellite scenes. Our results confirm that hyperspectral data, particularly in the SWIR domain, provide sufficient spectral detail to distinguish *Tillandsia* from spectrally similar background materials, even at low fractional cover.

A key contribution of this work is the implementation of a dual-library strategy that combines field-based and image-derived endmembers in two distinct modeling scenarios. Field spectra provided high spectral purity and were well suited for local analysis under controlled conditions, while the image-based library enabled reliable FVC estimation at the regional scale due to its radiometric compatibility with the satellite data. This approach highlights a fundamental trade-off in spectral library design and underscores the importance of tailoring endmember selection to the spectral and spatial characteristics of the target application.

Validation using ultra-high-resolution reference data and stratified regression analyses confirmed the accuracy of our FVC estimates across spatial scales. Targeted evaluation in confirmed *Tillandsia* areas helped mitigate statistical distortions caused by zero-inflated data and provided ecologically meaningful accuracy measures. These results demonstrate the operational feasibility of EnMAP for monitoring sparse vegetation under realistic desert conditions.

Building on these findings, future work will focus on extending the mapping of *Tillandsia* across the entire Atacama Desert and estimating its above-ground biomass. These efforts will be supported by improved ground-truth data collection and sampling strategies, including the use of a UAV-based narrow-band camera (Jenal et al. 2019) to target the *Tillandsia*-specific absorption features, thereby refining spectral analysis. Incorporating structural plant data using advanced tools such as SLAM LiDAR systems will enhance biomass estimation by providing detailed three-dimensional insights into the plant morphology.

In sum, this study presents a transferable framework for the remote sensing of low-signal vegetation in extreme environments. Our results show that hyperspectral imaging enables the reliable detection of *Tillandsia landbeckii*, thus making this previously undetectable species visible.

# 7 Appendix

**Table 4** Pre- and post-fitted regression metrics for model performance in the local area at 30 m resolution, with all error metrics expressed in percent; the best model is highlighted

| | Model | Area | MAE (pre) | MAE (post) | rMAE (pre) | rMAE (post) | RMSE (pre) | RMSE (post) |
|---|---|---|---|---|---|---|---|---|
| 30 m | *SUnSAL* | *Local* | *4.4* | *4.3* | *14.4* | *14.1* | *5.7* | *5.4* |
| | CLSUnSAL | Local | 9.7 | 6.7 | 31.9 | 22.0 | 11.4 | 8.0 |
| | $S^2$WSU | Local | 8.0 | 6.7 | 26.4 | 22.1 | 9.8 | 8.1 |
| | MUA SLIC | Local | 11.0 | 3.9 | 36.3 | 13.0 | 12.1 | 5.2 |
| | SUnCNN | Local | 19.3 | 6.0 | 63.4 | 19.6 | 20.7 | 7.6 |
| | SUnAA | Local | 17.3 | 5.6 | 57.0 | 18.5 | 18.7 | 7.2 |

**Table 5** Pre- and post-fitted regression metrics for model performance in the local area at 60 m resolution, with all error metrics expressed in percent; the best-performing model is highlighted

| | Model | Area | MAE (pre) | MAE (post) | rMAE (pre) | rMAE (post) | RMSE (pre) | RMSE (post) |
|---|---|---|---|---|---|---|---|---|
| 60 m | *SUnSAL* | *Local* | *3.1* | *2.8* | *15.3* | *14.3* | *4.3* | *3.7* |
| | CLSUnSAL | Local | 7.7 | 4.9 | 38.5 | 24.8 | 9.2 | 5.7 |
| | $S^2$WSU | Local | 6.0 | 5.3 | 30.3 | 26.7 | 7.4 | 6.4 |
| | MUA SLIC | Local | 10.1 | 2.9 | 50.7 | 14.6 | 10.8 | 3.9 |
| | SUnCNN | Local | 19.6 | 5.4 | 98.6 | 27.3 | 20.7 | 6.6 |
| | SUnAA | Local | 17.5 | 5.2 | 88.1 | 26.2 | 18.7 | 6.4 |

**Table 6** Pre- and post-fitted regression metrics showing model performance for regional areas at 30 m resolution. All error metrics are expressed in percent. The best model is highlighted.

| | Model | Area | MAE (pre) | MAE (post) | rMAE (pre) | rMAE (post) | RMSE (pre) | RMSE (post) |
|---|---|---|---|---|---|---|---|---|
| 30 m | *SUnSAL* | *Regional* | *0.9* | *1.4* | *1.9* | *2.9* | *2.6* | *2.5* |
| | CLSUnSAL | Regional | 1.0 | 1.3 | 2.2 | 2.9 | 2.2 | 2.1 |
| | $S^2$WSU | Regional | 1.2 | 1.6 | 2.6 | 3.6 | 3.1 | 2.9 |
| | MUA SLIC | Regional | 1.1 | 1.5 | 2.3 | 3.2 | 2.7 | 2.5 |
| | SUnCNN | Regional | 1.2 | 1.0 | 2.0 | 1.7 | 2.7 | 1.7 |
| | SUnAA | Regional | – | – | – | – | – | – |

**Table 7** Pre- and post-fitted regression metrics showing model performance for regional areas at 60 m resolution. All error metrics are expressed in percent. The best model is highlighted.

| | Model | Area | MAE (pre) | MAE (post) | rMAE (pre) | rMAE (post) | RMSE (pre) | RMSE (post) |
|---|---|---|---|---|---|---|---|---|
| 60 m | *SUnSAL* | *Regional* | *0.9* | *1.2* | *2.1* | *2.9* | *2.3* | *2.2* |
| | CLSUnSAL | Regional | 0.9 | 1.1 | 2.5 | 3.0 | 2.0 | 1.8 |
| | $S^2$WSU | Regional | 1.2 | 1.5 | 3.1 | 4.0 | 2.8 | 2.6 |
| | MUA SLIC | Regional | 1.0 | 1.3 | 2.5 | 3.3 | 2.4 | 2.2 |
| | SUnCNN | Regional | 1.2 | 1.0 | 3.6 | 3.1 | 2.4 | 1.6 |
| | SUnAA | Regional | – | – | – | – | – | – |

**Table 8** Pre- and post-fitted regression metrics showing model performance for regional areas at 30 m resolution with masked data. All error metrics are expressed in percent. The best model is highlighted.

| | Model | Area | MAE (pre) | MAE (post) | rMAE (pre) | rMAE (post) | RMSE (pre) | RMSE (post) |
|---|---|---|---|---|---|---|---|---|
| 30 m | SUnSAL | Regional | 3.4 | 3.6 | 7.3 | 7.8 | 5.1 | 4.8 |
| | *CLSUnSAL* | *Regional* | *2.7* | *2.7* | *6.0* | *6.1* | *4.0* | *3.7* |
| | $S^2$WSU | Regional | 3.7 | 3.8 | 8.0 | 8.2 | 5.4 | 4.9 |
| | MUA SLIC | Regional | 3.5 | 3.6 | 7.5 | 7.8 | 5.1 | 4.7 |
| | SUnCNN | Regional | 4.1 | 1.4 | 14.6 | 5.1 | 6.7 | 2.2 |
| | SUnAA | Regional | – | – | – | – | – | – |

**Table 9** Pre- and post-fitted regression metrics showing model performance for regional areas at 60 m resolution with masked data. The best model is highlighted.

| | Model | Area | MAE (pre) | MAE (post) | rMAE (pre) | rMAE (post) | RMSE (pre) | RMSE (post) |
|---|---|---|---|---|---|---|---|---|
| 60 m | SUnSAL | Regional | 2.4 | 2.7 | 6.0 | 6.7 | 4.0 | 3.8 |
| | *CLSUnSAL* | *Regional* | *1.8* | *1.9* | *4.7* | *5.0* | *2.8* | *2.7* |
| | $S^2$WSU | Regional | 2.6 | 2.9 | 7.0 | 7.6 | 4.2 | 3.9 |
| | MUA SLIC | Regional | 2.5 | 2.7 | 6.3 | 6.9 | 4.1 | 3.7 |
| | SUnCNN | Regional | 3.0 | 1.3 | 16.5 | 7.3 | 5.0 | 1.9 |
| | SUnAA | Regional | – | – | – | – | – | – |

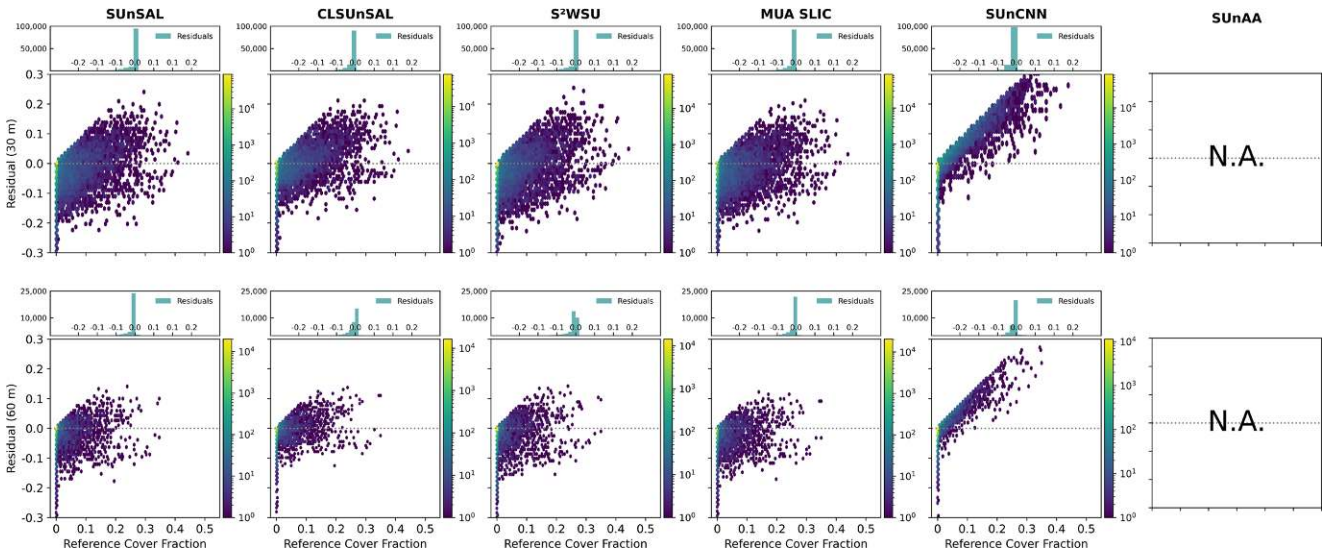


**Fig. 16** Residual plots for six models at 30 m (top) and 60 m (bottom) resolution. Residuals (reference—prediction) are plotted against reference cover fraction. Density is shown via hexbin shading; marginal histograms display residual distributions

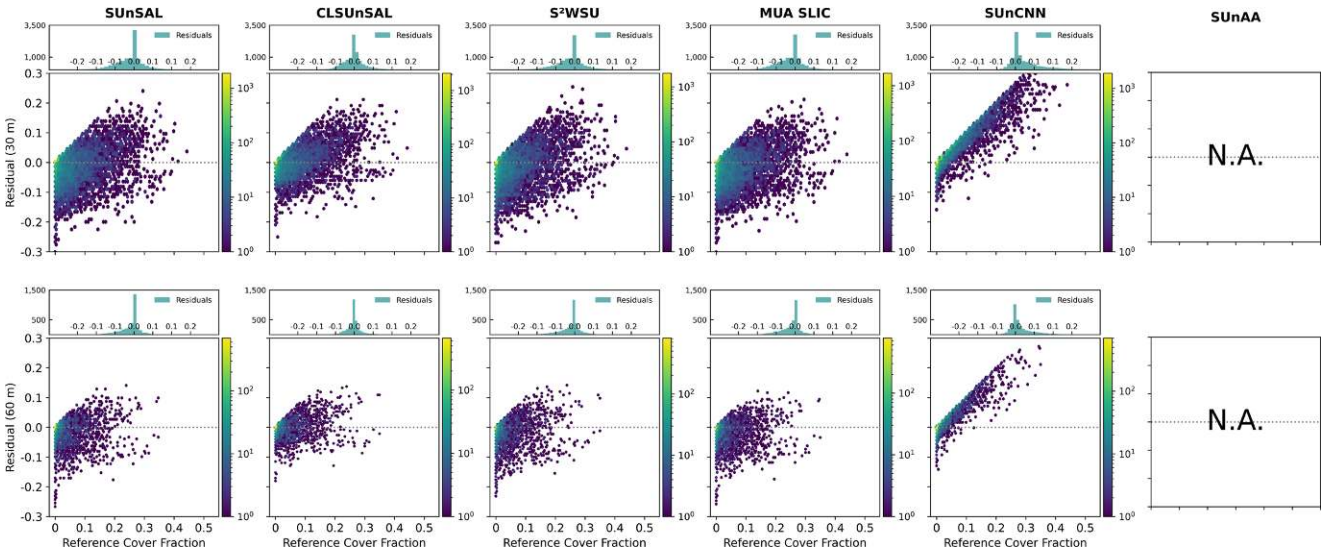


**Fig. 17** Residual plots for six models at 30 m (top) and 60 m (bottom) resolution (masked). Residuals (reference—prediction) are plotted against reference cover fraction. Density is shown via hexbin shading; marginal histograms display residual distributions

**Funding** This research is affiliated with the Collaborative Research Centre (CRC) 1211 "Earth—Evolution at the Dry Limit" (Grant-No.: 268236062), funded by the German Research Foundation (Deutsche Forschungsgemeinschaft, DFG), Germany. The project examines the evolutionary relationships between biota and Earth's surface processes in hyper-arid and arid environments. We would like to thank Alexandre Zouaoui, co-author of the HySUPP Python package, for his constant support concerning challenges in using the package.

**Funding** Open Access funding enabled and organized by Projekt DEAL.

**Conflict of interest** F. Reddig, C. Hütt, A. Jenal, J. Wolf and G. Bareth declare that they have no competing interests.

**Open Access** This article is licensed under a Creative Commons Attribution 4.0 International License, which permits use, sharing, adaptation, distribution and reproduction in any medium or format, as long as you give appropriate credit to the original author(s) and the source, provide a link to the Creative Commons licence, and indicate if changes were made. The images or other third party material in this article are included in the article's Creative Commons licence, unless indicated otherwise in a credit line to the material. If material is not included in the article's Creative Commons licence and your intended use is not permitted by statutory regulation or exceeds the permitted use, you will need to obtain permission directly from the copyright holder. To view a copy of this licence, visit http://creativecommons.org/licenses/by/4.0/.

## References

Adams JB, Gillespie AR (2006) Remote sensing of landscapes with spectral images: a physical modeling approach, 1st edn. Cambridge University Press, Cambridge https://doi.org/10.1017/CBO9780511617195

Adams JB, Smith MO, Johnson PE (1986) Spectral mixture modeling: a new analysis of rock and soil types at the viking lander 1 site. J Geophys Res Solid Earth 91(B8):8098–8112. https://doi.org/10.1029/JB091iB08p08098

Asner GP, Heidebrecht KB (2002) Spectral unmixing of vegetation, soil and dry carbon cover in arid regions: comparing multispectral and hyperspectral observations. Int J Remote Sens 23(19):3939–3958. https://doi.org/10.1080/01431160110115960

Bareth G, Hütt C (2023) Evaluation of direct RTK-georeferenced UAV images for crop and pasture monitoring using polygon grids. PFG 91(6):471–483. https://doi.org/10.1007/s41064-023-00259-7

Bareth G, Bendig J, Tilly N et al (2016) A comparison of UAV- and TLS-derived plant height for crop monitoring: using polygon grids for the analysis of crop surface models (CSMs). PFG 2016(2):85–94. https://doi.org/10.1127/pfg/2016/0289

Bioucas-Dias JM, Figueiredo MAT (2010) Alternating direction algorithms for constrained sparse regression: application to hyperspectral unmixing. In: 2010 2nd workshop on hyperspectral image and signal processing: evolution in remote sensing. IEEE, Reykjavik, pp 1–4 https://doi.org/10.1109/WHISPERS.2010.5594963

Borsoi RA, Imbiriba T, Bermudez JCM et al (2019) A fast multiscale spatial regularization for sparse hyperspectral unmixing. IEEE Geosci Remote Sens Lett 16(4):598–602. https://doi.org/10.1109/LGRS.2018.2878394

Borsoi RA, Imbiriba T, Bermudez JCM et al (2021) Spectral variability in hyperspectral data unmixing: a comprehensive review. IEEE Geosci Remote Sens Mag 9(4):223–270. https://doi.org/10.1109/MGRS.2021.3071158

Bull AT, Andrews BA, Dorador C et al (2018) Introducing the Atacama desert. Antonie Van Leeuwenhoek 111(8):1269–1272. https://doi.org/10.1007/s10482-018-1100-2

Cavalli RM (2023) Spatial validation of spectral unmixing results: a systematic review. Remote Sens 15(11):2822. https://doi.org/10.3390/rs15112822

Chabrillat S, Guanter L, Kaufmann H et al (2022) EnMAP Science Plan. Tech. rep. GFZ Data Services https://doi.org/10.48440/ENMAP.2022.001

Chakravortty S (2024) Non-linear spectral unmixing of hyperspectral data, 1st edn. CRC Press, Boca Raton

Congalton RG, Green K (2019) Assessing the accuracy of remotely sensed data: principles and practices, 3rd edn. CRC Press https://doi.org/10.1201/9780429052729

Cooper S, Okujeni A, Pflugmacher D et al (2021) Combining simulated hyperspectral EnMAP and Landsat time series for forest aboveground biomass mapping. Int J Appl Earth Obs Geoinf 98:102307. https://doi.org/10.1016/j.jag.2021.102307

Del Río C, Lobos-Roco F, Latorre C et al (2021) Spatial distribution and interannual variability of coastal fog and low clouds cover in the hyperarid Atacama Desert and implications for past and present Tillandsia landbeckii ecosystems. Plant Syst Evol 307(5):58. https://doi.org/10.1007/s00606-021-01782-z

Dennison PE, Qi Y, Meerdink SK et al (2019) Comparison of methods for modeling fractional cover using simulated satellite hyperspectral Imager spectra. Remote Sens 11(18):2072. https://doi.org/10.3390/rs11182072

Dunai TJ, González López GA, Juez-Larré J (2005) Oligocene–Miocene age of aridity in the Atacama Desert revealed by exposure dating of erosion-sensitive landforms. Geology 33(4):321. https://doi.org/10.1130/G21184.1

Eshel G, Araus V, Undurraga S et al (2021) Plant ecological genomics at the limits of life in the Atacama Desert. Proc Natl Acad Sci USA 118(46):e2101177118. https://doi.org/10.1073/pnas.2101177118

ESRI (2024) Image Classification Wizard—ArcGIS Pro | Documentation. https://pro.arcgis.com/en/pro-app/latest/help/analysis/image-analyst/the-image-classification-wizard.htm. Accessed 11 Nov 2024

European Space Agency (ESA) (2025) Sentinel-2 mission overview. Tech. rep., SentiWiki—Copernicus. https://sentiwiki.copernicus.eu/web/sentinel-2. Accessed 28 Mar 2025

Gelman A, Hill J (2007) Data analysis using regression and multilevel/hierarchical models. Cambridge University Press, Cambridge https://doi.org/10.1017/CBO9780511790942

U.S. Geological Survey (USGS) (2025) Landsat 8. Tech. rep., U.S. Geological Survey. https://www.usgs.gov/landsat-missions/landsat-8. Accessed 28 Mar 2025

German Aerospace Center (DLR) (2024) Level 1C Processor Geometric Correction: Technical Note (EN-PCV-TN-5006). Tech. rep

Guerschman JP, Hill MJ, Renzullo LJ et al (2009) Estimating fractional cover of photosynthetic vegetation, non-photosynthetic vegetation and bare soil in the Australian tropical savanna region upscaling the EO-1 Hyperion and MODIS sensors. Remote Sens Environ 113(5):928–945. https://doi.org/10.1016/j.rse.2009.01.006

Hampton B (2001) Early-middle Tertiary deposition in the Corque syncline, Altiplano plateau, Bolivia. Master of science. Louisiana State University, Agricultural and Mechanical College https://doi.org/10.31390/gradschool_theses.3615

Haslam R, Borland A, Maxwell K et al (2003) Physiological responses of the CAM epiphyteTillandsia usneoides L. (Bromeliaceae) to variations in light and water supply. J Plant Physiol 160(6):627–634. https://doi.org/10.1078/0176-1617-00970

Hesse R (2012) Spatial distribution of and topographic controls on Tillandsia fog vegetation in coastal southern Peru: remote sensing and modelling. J Arid Environ 78:33–40. https://doi.org/10.1016/j.jaridenv.2011.11.006

Houston J, Hartley AJ (2003) The central Andean west-slope rainshadow and its potential contribution to the origin of hyper-aridity in the Atacama Desert. Int J Climatol 23(12):1453–1464. https://doi.org/10.1002/joc.938

Iordache MD, Bioucas-Dias JM, Plaza A (2014) Collaborative sparse regression for hyperspectral unmixing. IEEE Trans Geosci Remote Sens 52(1):341–354. https://doi.org/10.1109/TGRS.2013.2240001

Jaeschke A, Böhm C, Merklinger FF et al (2019) Variation in δ15N of fog-dependent Tillandsia ecosystems reflect water availability across climate gradients in the hyperarid Atacama Desert. Glob Planet Change 183:103029. https://doi.org/10.1016/j.gloplacha.2019.103029

Jaeschke A, Böhm C, Schween JH et al (2024) Evaluating the isotopic composition of leaf organic compounds in fog-dependent Tillandsia landbeckii across the coastal Atacama Desert: Implications for hydroclimate reconstructions at the dry limit. Glob Planet Change 235:104393. https://doi.org/10.1016/j.gloplacha.2024.104393

Jenal A, Bareth G, Bolten A et al (2019) Development of a VNIR/SWIR multispectral imaging system for vegetation monitoring with unmanned aerial vehicles. Sensors 19(24):5507. https://doi.org/10.3390/s19245507

Jimenez-Rodriguez S, Dettinger M, Quade J et al (2021) Paleoaltimetry of the Western Andes in Northern Chile (∼18.5–19.5°S). Am J Sci 321(5):491–533. https://doi.org/10.2475/05.2021.01

Juola J, Tuominen S, Haapanen R et al (2024) Comparison of contemporaneous sentinel-2 and enmap data for vegetation index-based estimation of leaf area index and canopy closure of a boreal forest. Int J Remote Sens 45(13):4177–4205. https://doi.org/10.1080/01431161.2023.2253545

Kale VK, Solankar MMB, Nalawade D (2019) Hyperspectral endmember extraction techniques. In: Chen J, Song Y, Li H (eds) Processing and analysis of hyperspectral data. IntechOpen, https://doi.org/10.5772/intechopen.88910

Keshava N, Mustard JF (2002) Spectral unmixing. IEEE Signal Process Mag 19(1):44–57. https://doi.org/10.1109/79.974727

Knief U, Forstmeier W (2021) Violating the normality assumption may be the lesser of two evils. Behav Res 53:2576–2590. https://doi.org/10.3758/s13428-021-01587-5

Koch MA, Kleinpeter D, Auer E et al (2019) Living at the dry limits: ecological genetics of Tillandsia landbeckii lomas in the Chilean Atacama desert. Plant Syst Evol 305(10):1041–1053. https://doi.org/10.1007/s00606-019-01623-0

Koch MA, Kiefer C, Möbus J et al (2022) Range expansion and contraction of Tillandsia landbeckii lomas in the hyperarid Chilean Atacama Desert indicates ancient introgression and geneflow. Perspect Plant Ecol Evol Syst 56:125689. https://doi.org/10.1016/j.ppees.2022.125689

Latorre C, González AL, Quade J et al (2011) Establishment and formation of fog-dependent Tillandsia landbeckii Dunes in the Atacama Desert: Evidence from Radiocarbon and Stable Isotopes. J Geophys Res 116(G3):G3033. https://doi.org/10.1029/2010JG001521

Liang S, Wang J (2020) Chapter 12—Fractional vegetation cover. In: Advanced remote sensing, 2nd edn. Academic Press, pp 477–510 https://doi.org/10.1016/B978-0-12-815826-5.00012-X

Males J, Griffiths H (2017) Functional types in the Bromeliaceae: relationships with drought-resistance traits and bioclimatic distributions. Funct Ecol 31(10):1868–1880. https://doi.org/10.1111/1365-2435.12900

Maßon LA, Riedesel S, Zander A et al (2024) Testing the applicability of standardised growth curves for chemically heterogeneous single-grain feldspars from the Atacama Desert, Chile. Quat Geochronol 83:101585. https://doi.org/10.1016/j.quageo.2024.101585

Mikulane S, Siegmund A, Río CD et al (2022) Remote sensing based mapping of Tillandsia fields—A semi-automatic detection approach in the hyperarid coastal Atacama Desert, northern Chile. J Arid Environ 205:104821. https://doi.org/10.1016/j.jaridenv.2022.104821

Moat J, Orellana-Garcia A, Tovar C et al (2021) Seeing through the clouds—mapping desert fog oasis ecosystems using 20 years of MODIS imagery over Peru and Chile. Int J Appl Earth Obs Geoinf 103:102468. https://doi.org/10.1016/j.jag.2021.102468

Pervin R, Robeson SM, MacBean N (2022) Fusion of airborne hyperspectral and LiDAR canopy-height data for estimating fractional cover of tall woody plants, herbaceous vegetation, and other soil cover types in a semi-arid savanna ecosystem. Int J Remote Sens 43(10):3890–3926. https://doi.org/10.1080/01431161.2022.2105176

Pinto R, Barría I, Marquet P (2006) Geographical distribution of Tillandsia lomas in the Atacama Desert, northern Chile. J Arid

Environ 65(4):543–552. https://doi.org/10.1016/j.jaridenv.2005.08.015

Plaza A, Martinez P, Perez R et al (2002) Spatial/spectral endmember extraction by multidimensional morphological operations. IEEE Trans Geosci Remote Sens 40(9):2025–2041. https://doi.org/10.1109/TGRS.2002.802494

Plaza A, Martín G, Plaza J et al (2011) Recent developments in endmember extraction and spectral Unmixing. In: Prasad S, Bruce LM, Chanussot J (eds) Optical remote sensing. Springer, Berlin, Heidelberg, pp 235–267 https://doi.org/10.1007/978-3-642-14212-3_12

Plaza J, Hendrix EMT, García I et al (2012) On endmember identification in hyperspectral images without pure pixels: a comparison of algorithms. J Math Imaging Vis 42:163–175. https://doi.org/10.1007/s10851-011-0276-0

Rasti B, Koirala B (2022) SunCNN: sparse unmixing using unsupervised convolutional neural network. IEEE Geosci Remote Sens Lett 19:1–5. https://doi.org/10.1109/LGRS.2021.3100992

Rasti B, Zouaoui A, Mairal J et al (2023) SUnAA: sparse unmixing using archetypal analysis. IEEE Geosci Remote Sens Lett 20:1–5. https://doi.org/10.1109/LGRS.2023.3284221

Rasti B, Zouaoui A, Mairal J et al (2024) Image processing and machine learning for hyperspectral unmixing: an overview and the HySUPP python package. IEEE Trans Geosci Remote Sens 62:1–31. https://doi.org/10.1109/TGRS.2024.3393570

Rundel PW, Palma B, Dillon MO et al (1997) Tillandsia landbeckii in the coastal Atacama desert of northern Chile. Rev Chil Hist Nat 70:341–349

Schowengerdt RA (2007) Thematic classification. In: Remote sensing. Elsevier, pp 387–XXXIII https://doi.org/10.1016/B978-012369407-2/50012-7

Schwieder M, Leitão P, Suess S et al (2014) Estimating fractional shrub cover using simulated EnMAP data: a comparison of three machine learning regression techniques. Remote Sens 6(4):3427–3445. https://doi.org/10.3390/rs6043427

Theiler J, Ziemann A, Matteoli S et al (2019) Spectral variability of remotely sensed target materials: causes, models, and strategies for mitigation and robust exploitation. IEEE Geosci Remote Sens Mag 7(2):8–30. https://doi.org/10.1109/MGRS.2019.2890997

Verrelst J, Halabuk A, Atzberger C et al (2023) A comprehensive survey on quantifying non-photosynthetic vegetation cover and biomass from imaging spectroscopy. Ecol Indic 155:110911. https://doi.org/10.1016/j.ecolind.2023.110911

Wolf N, Siegmund A, Del Río C et al (2016) Remote sensing-based detection and spatial pattern analysis for geo-ecological niche modeling of Tillandsia spp. in the Atacama, Chile. In: The international archives of the photogrammetry, remote sensing and spatial information sciences, pp 251–256 https://doi.org/10.5194/isprs-archives-XLI-B2-251-2016

Zare A, Ho KC (2014) Endmember variability in hyperspectral analysis: addressing spectral variability during spectral unmixing. IEEE Signal Process Mag 31(1):95–104. https://doi.org/10.1109/MSP.2013.2279177

Zhang S, Li J, Li HC et al (2018) Spectral–spatial weighted sparse regression for hyperspectral image unmixing. IEEE Trans Geosci Remote Sens 56(6):3265–3276. https://doi.org/10.1109/TGRS.2018.2797200

Zhou Y, Wetherley EB, Gader PD (2020) Unmixing urban hyperspectral imagery using probability distributions to represent endmember variability. Remote Sens Environ 246:111857. https://doi.org/10.1016/j.rse.2020.111857